

# GreenRFM: Toward a resource-efficient radiology foundation model

Yingtai Li<sup>\*1,2</sup>, Shuai Ming<sup>\*3</sup>, Mingyue Zhao<sup>1,2</sup>, Haoran Lai<sup>1,2</sup>, Rongsheng Wang<sup>1,2</sup>, Rui Zhou<sup>1,2</sup>, Rundong Wang<sup>1,2</sup>, Yujia Li<sup>4,5</sup>, Wei Wei<sup>†3</sup>, and Shaohua Kevin Zhou<sup>†1,2,6,7</sup>

<sup>1</sup>School of Biomedical Engineering, Division of Life Sciences and Medicine, University of Science and Technology of China (USTC), Hefei, Anhui, 230026, China

<sup>2</sup>Center for Medical Imaging, Robotics, Analytic Computing & Learning (MIRACLE), Suzhou Institute for Advanced Research, USTC, Suzhou, Jiangsu, 215123, China

<sup>3</sup>Department of Radiology, The First Affiliated Hospital of USTC, Division of Life Sciences and Medicine, USTC, Hefei, Anhui, 230001, China

<sup>4</sup>Key Laboratory of Intelligent Information Processing of Chinese Academy of Sciences (CAS), Institute of Computing Technology, CAS

<sup>5</sup> University of Chinese Academy of Sciences

<sup>6</sup>Jiangsu Provincial Key Laboratory of Multimodal Digital Twin Technology, Suzhou, Jiangsu, 215123, China

<sup>7</sup>State Key Laboratory of Precision and Intelligent Chemistry, USTC, Hefei, Anhui, 230026, China

## Abstract

The development of radiology foundation models (RFMs) is hindered by a reliance on brute-force scaling. Existing approaches often directly translate methods for natural images, which prioritize scale over precision and hence lead to brittle and expensive models in clinical practice. To address this, we present a resource-efficient pre-training framework, GreenRFM, that achieves state-of-the-art performance. Our framework ensures robust generalization across diverse patient populations and imaging protocols, reducing computational requirements by orders of magnitude while surpassing complex, parameter-heavy models. These capabilities stem from principled supervision design that aims to maximally utilize supervisory signals via More distilled, Ubiquitous, Semantic-enforcing, and Task-aligning (MUST) supervision, rather than simply piling up the quantity of training data. We offer two GreenRFM configurations: (i) a performant model that establishes a new state-of-the-art using a single 24GB GPU within 24 hours, and (ii) a lightweight model that matches existing benchmarks with 6GB VRAM in 4 hours. We conduct extensive experiments using over 200,000 images from four institutions and of two modalities. GreenRFMs achieve superior performances on chest and abdominal CT datasets, regardless of public or private benchmark, surpassing a range of baseline models. In addition, the results on internal musculoskeletal MRI images show that the same supervision principles transfer between different modalities. Our performance and efficiency challenge the “scale is all you need” dogma and democratize the equitable development of state-of-the-art RFMs for clinicians even on a laptop.

---

\*These authors contributed equally to this work. Email: liyingtai@mail.ustc.edu.cn

†Corresponding authors: Shaohua Kevin Zhou (skevinzhou@ustc.edu.cn) and Wei Wei (weill@ustc.edu.cn).

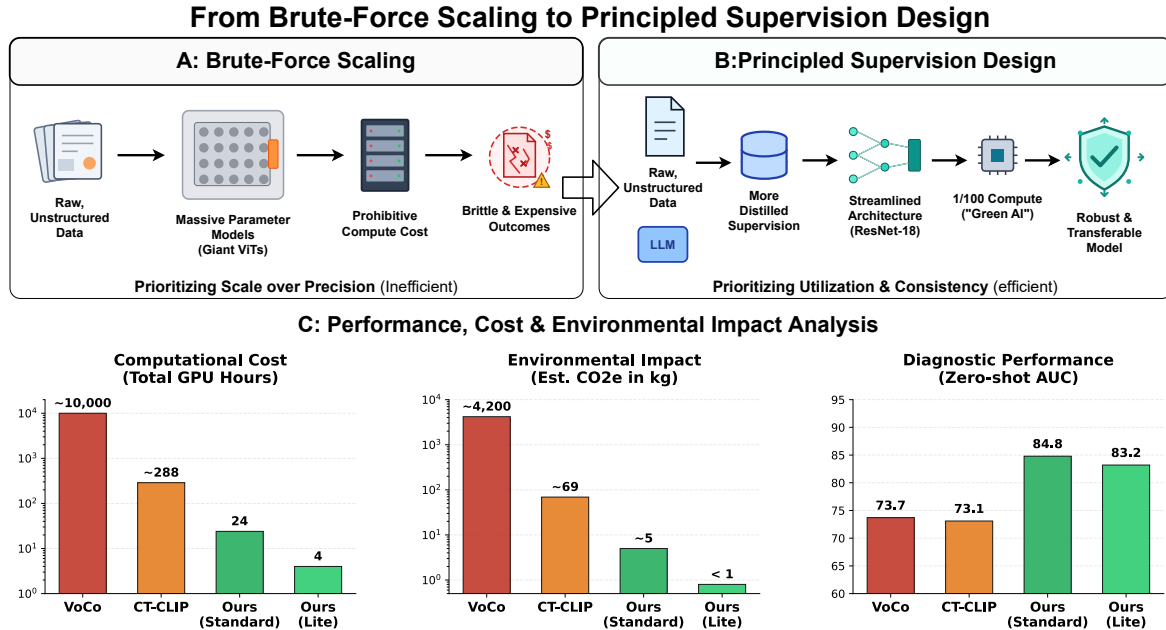


**Figure 1: A paradigm shift from brute-force scaling to principled supervision design.** **Panel A** illustrates the inefficiencies of current brute-force scaling approaches, which rely on massive noisy data and prohibitive compute to train parameter-heavy models, often resulting in brittle and expensive outcomes. **Panel B** depicts our proposed principled supervision design. By leveraging LLMs distillation to create structured “Silver-Standard” labels and employing a streamlined architecture (ResNet-18), we achieve a robust and transferable model with 1/100 of the compute resources. **Panel C** quantitatively demonstrates this advantage: our method (green) achieves superior diagnostic performance while reducing computational cost and environmental impact by orders of magnitude compared to massive (red) and standard (orange) baselines.

## Introduction

Medical imaging data serves as a cornerstone of modern medicine, providing a definitive modality for assessing human pathology. In particular, volumetric modalities like Computed Tomography (CT) and Magnetic Resonance Imaging (MRI) provide the critical 3D spatial context that underpins clinical decision-making across the healthcare spectrum, ranging from the early detection of occult malignancies to the rapid assessment of life-threatening trauma and cardiovascular emergencies [1–5]. Yet, this very success has precipitated a crisis: the explosive proliferation of imaging data has vastly outstripped the human capacity to interpret it. Radiologists, operating under the strain of increasing workloads and cognitive fatigue, face an overwhelming task that threatens diagnostic precision and patient safety. In this context, the advent of artificial intelligence (AI) offers a promising solution. Specifically, the rise of foundation models (FMs), paradigms built through large-scale pre-training on massive datasets to learn transferable representations, has ignited significant interest in translating these powerful models into the medical domain to automate diagnostic reasoning, democratize expert-level interpretation, and fundamentally reshape the workflow of modern radiology.

Radiology Foundation Models (RFMs) have emerged as the most promising paradigm for bridging pixel-level data and high-level clinical reasoning. By learning joint representations of medical imagery and the rich, descriptive narratives of radiology reports, it links the tacit visual knowledge of experts with explicit semantic signals. Beyond facilitating text-conditioned synthesis of realistic medical images [6–8], this cross-modal alignment enables interpreting medical images with natural language and retrieving semantically relevant cases. Furthermore, it has the potential to synergize the visual perception with the extensive world knowledge and reasoning prowess of Large Language Models (LLMs) [9–11], making the

construction of robust, scalable RFMs a prerequisite for ushering in the next era of medical artificial intelligence. Towards this goal, recent studies have started to exploit large collections of medical volumes and radiology reports for vision-language pre-training [12–14]. Most existing works treat paired images and reports as generic cross-modal data and optimize a CLIP-style [15] contrastive objective, positing that scaling alone will suffice [13].

However, the direct transplantation of generic vision-language pre-training paradigms into medical imaging faces profound challenges. While the “scale-is-all-you-need” philosophy has proven effective in the realm of general RFMs, its application to medical domains is constrained by the inherent scarcity of data compared to the internet-scale datasets available for general vision. Besides, the high-dimensional nature of medical scans imposes a computational and storage burden orders of magnitude higher than 2D snapshots, making efficiency paramount. More critically, recent systematic evaluations reveal that despite massive parameter counts, models often suffer from catastrophic failures in diagnostic accuracy and exhibit surprising brittleness when generalizing across diverse populations [16]. The core issue lies in a conceptual mismatch: standard contrastive objectives are designed to capture superficial semantic associations, whereas medical diagnosis demands a rigorous understanding of subtle pathological deviations. Consequently, the prevailing trend of pre-training gargantuan Vision Transformers (ViTs) for hundreds to thousands of epochs [17] represents a brute-force approach that is computationally inefficient and often yields fragile representations. Exemplifying this resource-intensive path, the recent VoCo framework [18] scales up to 1.2 billion parameters, requiring thousands of GPU hours on elite hardware (e.g., H800s). While demonstrating the potential of scale, such prohibitive resource requirements might restrict these advances to a few well-funded institutions, which aggregates inequity in model development [19]. More importantly, it masks the inefficiency of the underlying learning paradigm and hinders the methodological innovation necessary for pre-training efficient RFMs.

To resolve this impasse, we propose a fundamental paradigm shift: moving the locus of innovation from architectural complexity to supervision design. We introduce a principled supervision design framework that efficiently scales and maximizes the utility of supervisory signals. Our framework builds on our preliminary study [20] and substantially expands it through theoretical formalization and large-scale validation. Specifically, we conceptualize our design philosophy into four cardinal principles, abbreviated as MUST: *More distilled supervision*, which harnesses the reasoning power of modern LLMs to transform noisy reports into structured, high-fidelity diagnostic labels; *Ubiquitous supervision*, which injects explicit guidance into every component of the model—vision encoder, text encoder, and alignment space; *Semantic-enforcing supervision*, which posits that discriminative, independent modal representations must be semantically pre-trained before they can be effectively aligned; and *Task-aligning supervision*, which ensures that the architectural design and learning objectives of pre-training are strictly consistent with the clinical protocols of downstream applications.

Implementing this framework, we present a streamlined, resource-efficient two-stage pipeline that pre-trains a so-called GreenRFM that redefines the state-of-the-art. By shifting the focus from scaling parameters to maximizing supervision utility, we enable a standard, lightweight 3D ResNet-18 backbone to achieve unprecedented performance on zero-shot diagnosis and retrieval tasks, and demonstrates remarkable robustness to domain shifts and data heterogeneity. In stark contrast to massive baselines, we demonstrate that this model can surpass competitors in hours using only 1% of the data, and can be trained on a consumer-grade laptop (6GB VRAM). We validate this performance across a diverse cohort of over 200,000 images from four institutions, covering two large-scale benchmarks of CT-RATE and Merlin, and demonstrate a robust transferability to three external validation sets: RAD-ChestCT, AH-Chest and AH-Abd. To probe modality agnosticism, we additionally run

proof-of-concept validation on two private MRI cohorts (AH-Knee and AH-Spine) using the same supervision principles. By prioritizing clinically grounded supervision over architectural excess, this work offers more than just a new model. It provides a robust and sustainable blueprint for the next generation of RFMs — one that delivers on the promise of intelligent healthcare while remaining environmentally friendly and equitable to the broader community.

## Results

### A framework of principled supervision design maximizes data efficiency

To overcome the limitations of existing RFMs, which often rely on brute-force scaling of computation and parameters, we introduce a **principled supervision design** framework. This framework shifts the focus from architectural complexity to how to *efficiently scale* and *effectively utilize* supervisory signals. Our approach is built upon four design principles, abbreviated as MUST, that collectively maximize data efficiency.

**More distilled supervision** As illustrated in Fig. 2a, to bridge the gap between efficient-but-unscalable manual annotation and scalable-but-inefficient raw reports [21], we employ LLMs to distill unstructured radiology reports into massive, structured diagnostic labels that are crucial to downstream tasks. Furthermore, we explicitly model clinical uncertainty and missing data in this distillation process, creating a “silver-standard” of supervision that is both scalable and semantically dense. This allows us to bypass the need for expensive human curation while providing more, stronger learning signals than raw texts alone.

**Ubiquitous supervision:** Standard contrastive learning typically supervises only the alignment interface between vision and language, leaving the internal representations of each modality to be learned implicitly [15, 22]. Rather than this implicit learning, which might be inefficient, we inject supervision into every component of the architecture. We explicitly supervise the image encoder, the text encoder, and the shared alignment space across distinct training stages, as shown in Fig. 2b. This ensures that every component of the model is directly optimized for diagnostic discriminability, rather than relying on weak, indirect gradients to propagate back from the contrastive loss.

**Semantic-enforcing supervision:** The quality of unimodal representations dictates the performance upper bound, while alignment determines how much of that potential can be realized through another modality. Fundamentally, if the vision encoder cannot discriminate, say, a nodule from a vessel, no cross-modal alignment can rectify this semantic blindness. Therefore, we adopt a two-stage, semantic-enforcing pre-training strategy. In the first stage, we pre-train the vision and text encoders independently using the LLM-derived diagnostic labels. Only after these encoders have learned robust discriminative features do we proceed to the second stage of cross-modal alignment. This decoupling prevents the “tug-of-war” often seen in multi-task learning [23, 24] and ensures that alignment starts from a foundation of strong semantic understanding.

**Task-aligning supervision:** We meticulously align the architectural design, data domain, and learning objectives of pre-training with the downstream diagnosis task, as depicted in Fig. 2c. This principle extends beyond architectural choices, such as aligning pooling strategies and avoiding  $L_2$  normalization to preserve feature magnitude [25, 26], to enforce consistency by employing a domain-specific text encoder rooted in radiology rather than general biomedicine, and by prioritizing diagnostic supervision over generic visual descriptions. By minimizing the gap between how the model is trained and how it is applied, especially in downstream applications, we ensure that the learned representations translate seamlessly to radiology tasks.

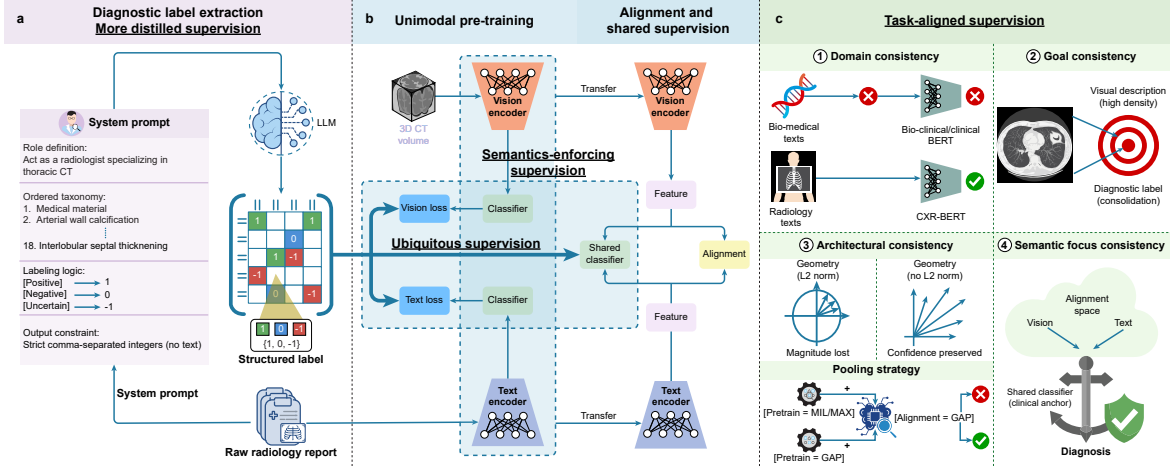


**Figure 2: Overview of the principled supervision design framework.** The framework is built upon four key principles to maximize data efficiency. **a, More distilled supervision:** An LLM distills noisy radiology reports into structured diagnostic labels (present, absent, uncertain), creating a scalable source of supervision. **b, Ubiquitous & semantics-enforcing supervision:** A two-stage training strategy is employed. First, vision and text encoders are independently pre-trained using the structured labels. Then, they are transferred to the alignment stage. Supervision is applied ubiquitously across distinct stages — to the vision encoder, text encoder, and the shared alignment space. **c, Task-aligning supervision:** This panel illustrates the design constraints applied to the training pipeline to enforce strict consistency with downstream diagnosis task: (1) Domain consistency via a radiology-specific text encoder; (2) Goal consistency by prioritizing diagnostic labels; (3) Architectural consistency by aligning pooling strategies and removing  $L_2$  normalization; and (4) Semantic focus consistency by anchoring the alignment space with a shared classifier.

### LLM-distilled diagnostic labels enable explicit diagnostic supervision

To address the challenge of scaling supervision without relying on expensive manual annotation (“More distilled supervision”, Principle 1), we utilize LLMs to distill unstructured radiology reports into structured diagnostic labels. This process represents a critical distillation step: raw reports are often replete with ambiguity, negation, and irrelevant administrative metadata, which act as noise during training. By prompting an LLM to extract the presence, absence, or uncertainty/missing of 18 specific abnormalities from the CT-RATE dataset reports, we effectively convert a noisy, unstructured signal into a dense, structured supervision target.

We rigorously evaluate the quality of these LLM-extracted labels against the official labels from the Merlin [27] dataset, which are manually reviewed to ensure accuracy. The results reveal a nuanced picture of LLM capability. While the model struggles to distinguish subtle “uncertain” mentions from definitive “negative” cases perfectly (Kappa=0.10), it achieves a remarkable agreement when these ambiguous cases are excluded (Kappa=0.94, F1=0.96) (Supplementary Table S4). Fig. S1 provides a detailed confusion matrix, which shows that most misclassifications occurred between “uncertain” (-1) and “negative” (0) labels, or between “uncertain” (-1) and “positive” (1) labels. Crucially, the confusion between definitive labels, e.g., “positive” (1) and “negative” (0), is extremely rare. This suggests that while fine-grained uncertainty detection remains a challenge for LLMs, they are highly effective in identifying definitive pathologies [28].

Crucially, we investigate whether these “silver-standard” labels — despite their inherent noise — could serve as an effective supervisory signal. The results are consistent with prior observations in Chest X-ray analysis [29], which indicate that handling uncertainty as binary targets often yields comparable performance and that deep neural networks exhibit strong robustness to label noise [30]. A vision encoder trained on these LLM-extracted labels achieves an AUC of 87.41% on the Merlin test set, slightly surpassing the performance of a model trained on the official curated labels (85.78%) (Supplementary Table S4). This is not

surprising given the extreme class imbalance inherent in medical datasets, where negative (0) and uncertain (-1) samples vastly outnumber positive (1) ones. Since the decision boundary in such imbalanced scenarios is primarily shaped by the minority positive class [31, 32], the noise within the majority classes (confusion between various negative states) has a negligible impact. This is further corroborated by the Merlin benchmark design, which balances positive and negative examples for evaluation to standardize the chance metric [27]. The superior performance on this balanced metric confirms that the model has effectively captured the critical diagnostic features from the minority positive samples, despite the noise in the dominant negative background. This finding challenges the dogma that only manually curated gold-standard annotations are suitable for training medical AI. It suggests that *the scalability of LLM-extracted labels* can compensate for their imperfect precision, effectively bridging the gap between raw text and structured clinical knowledge.

### Ubiquitous and semantics-enforcing supervision enhances representation and alignment

A key tenet of our framework is “Ubiquitous supervision” (Principle 2) — the idea that supervision should be injected into every component of the model rather than just the final alignment interface. We implement this via a two-stage training strategy that prioritizes “Semantic-enforcing supervision” (Principle 3). In the first stage, we independently pre-train the 3D CT encoder and the radiology report encoder using the LLM-derived diagnostic labels. In the second stage, we align these pre-trained encoders using a contrastive objective, while simultaneously maintaining a shared classifier to enforce diagnostic discriminability in the joint embedding space (Fig. 2b).

Our cumulative analysis demonstrates the value of this approach. Combined with a baseline CLIP-style model (AUC 80.6%), explicitly supervising the image encoder yields the *largest gain (+3.2%)*, confirming that strong single-modality representations are foundational. Extending supervision to the text encoder (+0.6%) and the shared alignment space (+0.4%) provides further improvements, culminating in a *final AUC of 84.8%* on CT-RATE (Table 4 and Fig.4a). Crucially, this performance is achieved with *remarkable efficiency*: our GreenRFM *converges in 10 epochs* (5 epochs of single-modality pretraining and 5 epochs of cross-modal alignment) with a standard 3D ResNet-18 backbone. With each report typically under 500 tokens, processing 10,000 samples costs less than one dollar. The standard high-performance version completes the entire supervised pre-training and alignment stages in **less than a day (24 hours) on a single RTX 3090 GPU (24GB VRAM)**. Furthermore, our lightweight version GreenRFM-L, designed for extreme resource constraints, maintains state-of-the-art performance while requiring only **6GB VRAM and 4 hours of training time**, making it accessible on consumer-grade laptops and improving equity in FM training.

We further analyze the data scaling properties of our method. As shown in Figure 3a, our GreenRFM exhibits *exceptional data efficiency* compared to previous works [27, 33]. Notably, our method matches the previous state-of-the-art using *less than 50% of the training data*. The performance exhibits a *log-linear growth*, indicating that the model has not yet saturated and possesses significant potential for further scaling. Crucially, as shown in Figure 3b, this trend extends to generalization: performance on external validation sets improves consistently with data scale, demonstrating superior data efficiency even in out-of-distribution scenarios.

Furthermore, we conduct a direct comparison with Multi-Task Learning (MTL), where representation learning and alignment are attempted simultaneously. The results are illuminating. The decoupled, two-stage training allows the vision encoder to achieve *significantly lower classification loss* (Fig. 3e), indicating that it learns more discriminative features when not distracted by the alignment objective. This superior initialization facilitates a *faster and more stable convergence* during the subsequent alignment phase (Fig. 3f). Given the known

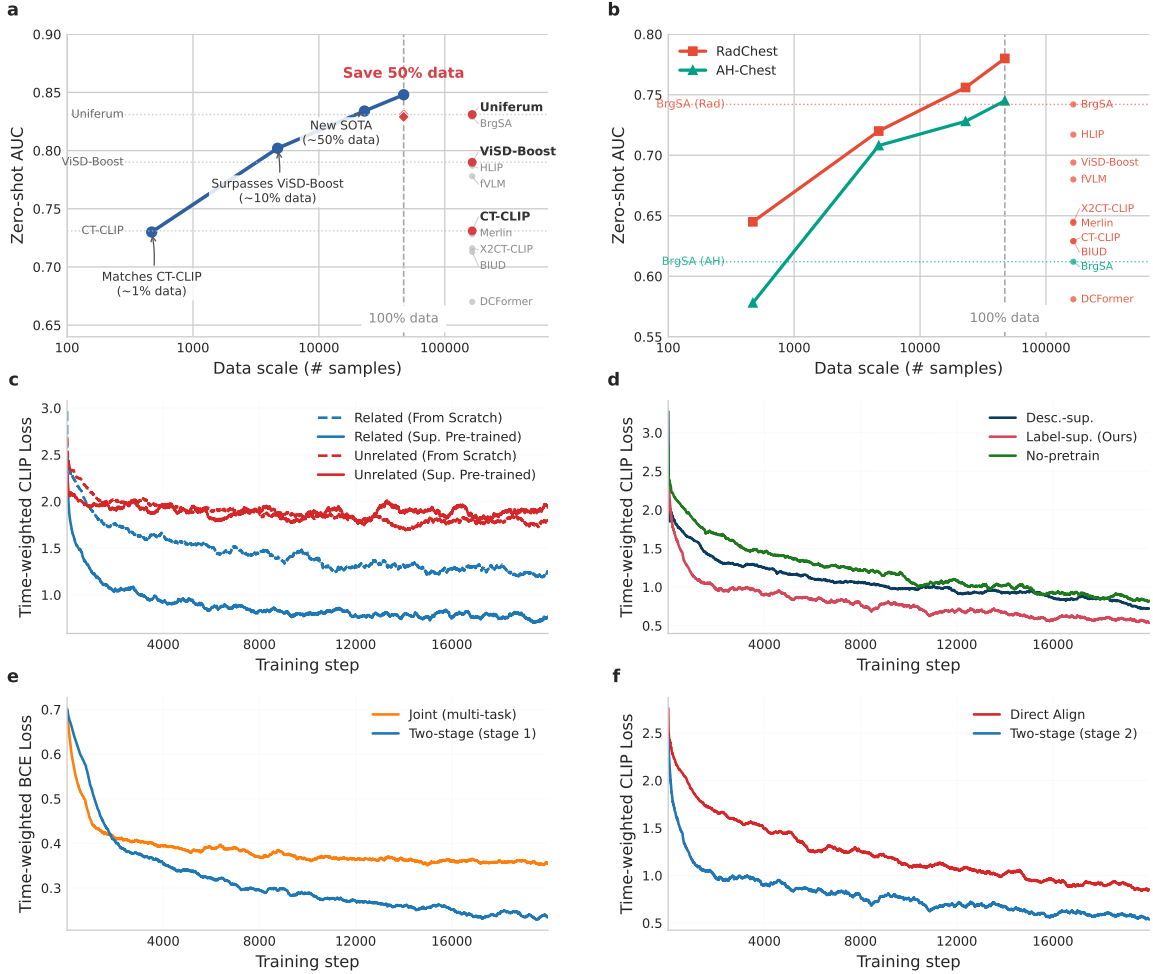


**Figure 3: Training dynamics, objective consistency, and data scaling.** **a**, Data scaling efficiency. Our method exhibits a significantly steeper scaling curve compared to previous works, matching state-of-the-art performance with less than 50% of the data. **b**, Generalization scaling law. The zero-shot performance on external validation sets (RAD-ChestCT and AH-Chest) improves consistently with training data scale. **c**, Alignment selectivity analysis. Comparing the alignment loss on label-related vs. label-unrelated report sentences, the supervised pre-trained model maintains similar alignment loss on sentences that do not contain diagnostic labels (label-unrelated). **d**, Impact of supervision type. Pre-training with diagnostic labels (ours) achieves lower alignment loss and faster convergence compared to using visual descriptions. **e**, Two-stage vs. Joint (multi-task) representation learning. The vision encoder achieves a significantly lower loss when trained independently (two-stage, stage 1) compared to when trained jointly with alignment objectives. **f**, Impact of two-stage training on alignment. The two-stage model converges faster and reaches a lower alignment loss compared to the direct aligning baseline.

sensitivity of zero-shot metrics to prompt engineering, we utilize this validation alignment loss (generalization error) as a robust, prompt-independent proxy for alignment quality. The consistently *lower loss achieved by GreenRFM* confirms that multi-task learning, by entangling competing objectives, can compromise the quality of single-modality representations, which in turn bottlenecks the final alignment performance. In contrast, our two-stage approach ensures that the alignment phase begins with high-quality features, leading to a more robust final model.

### Task-aligning supervision maximizes diagnostic utility

We discover that the alignment between pre-training objectives and downstream diagnostic protocols (“Task-aligning supervision”, Principle 4) is a critical determinant of performance.

We dissect this principle into four key aspects: domain consistency, supervision consistency, architectural consistency, and semantic focus consistency.

### **Domain-specific text encoder ensures semantic alignment**

We first validate the importance of using a domain-specific text encoder. As shown in Fig. 4, the domain-specific CXR-BERT [34], pre-trained specifically on radiology reports with a specialized tokenizer vocabulary, significantly outperforms broader biomedical models like BioClinicalBERT and ClinicalBERT (AUC 84.8% vs. 78.4% and 80.4%). This superiority stems from the alignment between the pre-training data (CXR report text) and the downstream task (CT report understanding). Generic biomedical models, despite being trained on vast amounts of literature, lack the specific granular understanding of radiology terminology required for precise alignment.

### **Diagnostic supervision outperforms visual descriptions**

We then investigate the impact of supervision type. We compare pre-training with diagnostic labels versus visual descriptions. To obtain scalable visual supervision, we employ an LLM to extract 11 distinct visual patterns from reports, covering density (e.g., high/low attenuation), morphology (e.g., patchy, reticular), and distribution (e.g., focal, diffuse). Contrary to the intuition that these explicit visual attributes might be more “vision-friendly,” we find that pre-training with diagnostic labels *significantly outperforms visual descriptions (AUC 84.8% vs. 81.3% on CT-RATE)* (Fig. 4). This suggests that for diagnostic tasks, supervision must be directly aligned with the disease concepts of interest (Fig. 3d). While visual descriptions capture texture, diagnostic labels capture the *clinical implication* of those textures.

### **Architectural consistency maximizes diagnostic utility**

Beyond supervisory signals, we investigate the impact of feature normalization and pooling strategies. First, we challenge the standard practice of  $L_2$  normalization. We posit that *feature magnitude encodes confidence or saliency* in supervised settings. Enforcing  $L_2$  normalization during pre-training degrades supervised performance (AUC 85.9% vs. 83.9%), and enforcing it during alignment disrupts the learned feature geometry, dropping downstream AUC to 81.7% (Fig. 4). *Removing  $L_2$  normalization ensures consistency* between stages, allowing the model to preserve magnitude-based confidence signals. Second, we align the pooling strategy. We show that using Global Average Pooling (GAP) throughout — matching the condition of zero-shot evaluation — results in *superior downstream performance (AUC 84.8% vs. 82.6%)* compared to MIL-based pooling (Fig. 4). This underscores the importance of minimizing the “*training-inference gap*”: architectural choices during pre-training must mirror final deployment conditions.

### **Semantic focus consistency via shared classifier**

Finally, we ensure *Semantic Focus Consistency* by integrating a shared classifier into the alignment stage, *continuing the precise diagnostic supervision initiated during the pre-training of unimodal encoder* (Fig. 2c). This ensures that the discriminative features learned in the first stage are explicitly preserved and prioritized in the joint embedding space, preventing them from being diluted by the generic contrastive objective. Quantitative ablation confirms the effectiveness of this design, showing that the addition of the shared classifier in the alignment stage improves the zero-shot AUC on CT-RATE from 84.4% to 84.8% (Fig 4a).

### **GreenRFM is robust and transferrable across diverse clinical scenarios**

#### **State-of-the-art performance on public benchmarks**

We validate our framework on three large-scale public benchmarks: CT-RATE (internal), RAD-ChestCT (external), and Merlin (internal). As summarized in Table 1, our method con-

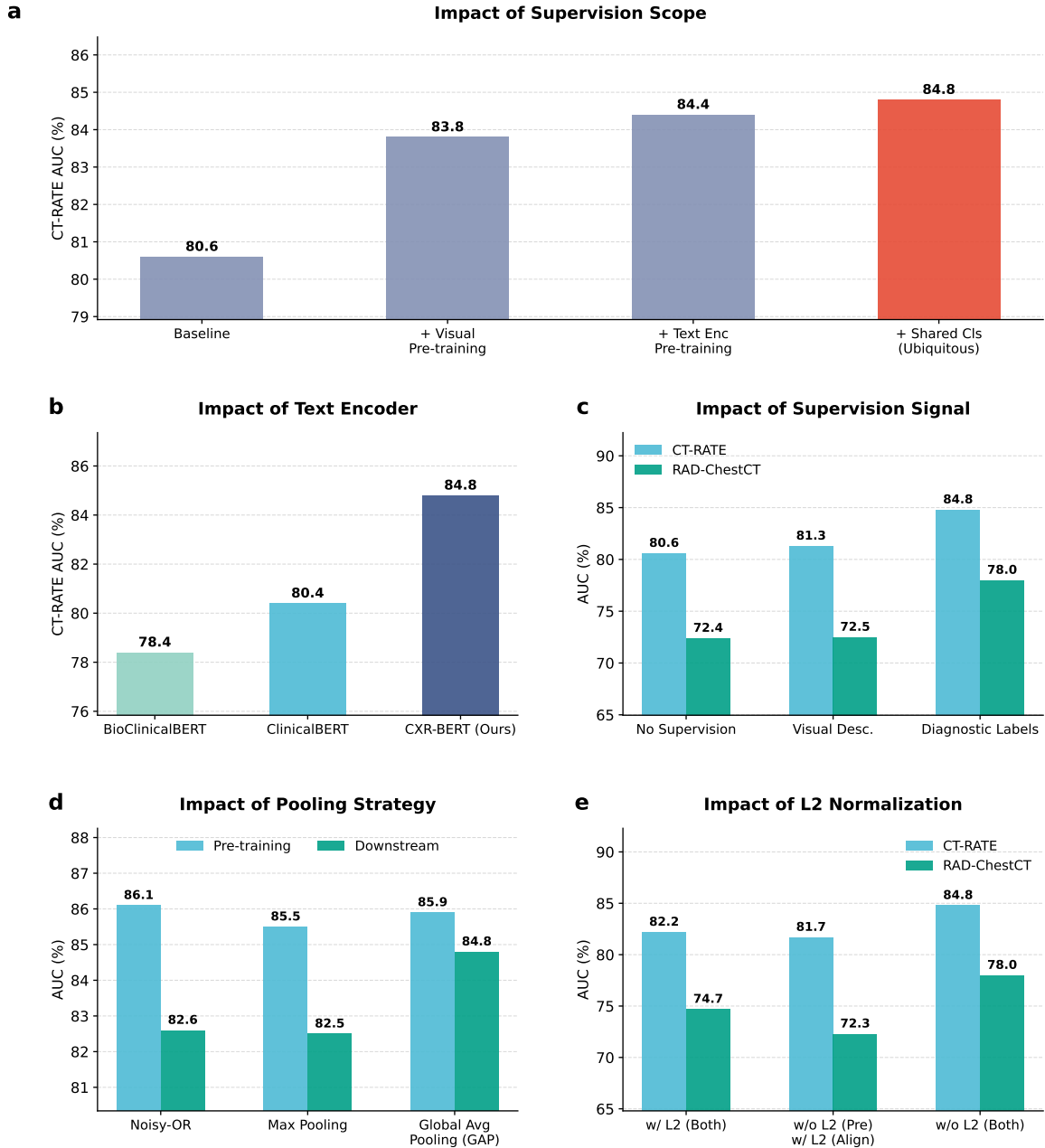


**Figure 4: Ablation studies on task-aligning supervision design.** **a**, Impact of supervision scope. Explicitly supervising every component (visual, text, and shared classifier) yields the best performance. **b**, Impact of text encoder. Domain-specific CXR-BERT outperforms general biomedical models. **c**, Impact of supervisory signal. Diagnostic labels provide stronger supervision than visual descriptions or no supervision. **d**, Impact of pooling strategy. Global Average Pooling (GAP) aligns best with downstream tasks compared to Noisy-OR or Max Pooling. **e**, Impact of  $L_2$  normalization. Removing  $L_2$  normalization preserves feature magnitude and improves performance.

sistently outperforms state-of-the-art approaches, including those relying on larger backbones, computationally intensive pre-training, or complex auxiliary tasks.

On the internal CT-RATE test set, we achieve an AUC of 84.8%, surpassing the previous best (Uniferum) of 83.1% and significantly outperforming standard CT-CLIP (73.1%). Notably, our method also outperforms the recent large-scale pre-training framework VoCo [18] (73.7%). This comparison is particularly striking given the immense disparity in model complexity and computational cost. VoCo relies on a *massive 1.2B-parameter model* and *160K training volumes*, consuming *over 10,000 GPU hours on 8× NVIDIA H800 GPUs*.

**Table 1: Zero-shot abnormality diagnosis performance comparison.** Comparison across internal (CT-RATE, Merlin) and external (RAD-ChestCT) validation benchmarks. Bold numbers denote the best performance. Our method consistently outperforms state-of-the-art approaches.

Method	CT-RATE				RAD-ChestCT				Merlin
	AUC	ACC	F1	Prec.	AUC	ACC	F1	Prec.	F1
OpenCLIP [35]	-	-	-	-	-	-	-	-	27.6 ± 1.4
BioMedCLIP [36]	-	-	-	-	-	-	-	-	28.5 ± 1.1
DCFormer [37]	67.0	62.4	66.8	28.6	58.1	55.8	60.8	29.9	-
X2CT-CLIP [38]	71.6	-	-	-	64.5	-	-	-	-
CT-CLIP [13]	73.1	66.8	70.7	32.3	62.9	59.5	64.2	33.6	-
VoCo [18]	73.7	-	-	-	-	-	-	-	-
BIUD [39]	71.3	68.1	71.6	33.8	62.9	60.6	65.2	33.7	-
Merlin [27]	72.8	67.2	70.9	33.7	64.4	61.9	66.3	34.8	74.1 ± 1.4
FVLM [33]	77.8	71.8	75.1	37.9	68.0	64.7	68.8	37.4	-
HLIP [40]	78.7	72.4	75.5	38.4	71.7	67.7	71.4	39.8	-
ViSD-Boost [41]	79.0	73.1	75.9	38.7	69.4	65.2	69.3	34.2	-
BrgSA [42]	82.9	77.0	79.3	43.2	74.2	68.6	72.0	42.2	-
Uniferum [43]	83.1	-	-	-	-	-	-	-	-
GreenRFM-L (ours)	83.2	77.1	79.4	43.2	76.5	71.0	74.1	44.6	82.1
<b>GreenRFM (ours)</b>	<b>84.8 ± 0.8</b>	<b>77.7 ± 0.9</b>	<b>80.0 ± 0.8</b>	<b>44.4 ± 1.6</b>	<b>78.0 ± 0.9</b>	<b>73.0 ± 0.9</b>	<b>75.7 ± 0.8</b>	<b>46.1 ± 1.3</b>	<b>84.3 ± 1.4</b>

In contrast, our model employs a **standard 3D ResNet-18 with only 33M parameters**—*approximately 3% of VoCo’s size*—without any specialized lightweight architectural designs. Remarkably, our framework is so data-efficient that it can *match VoCo’s performance using only 1% of the training data*. Even our lightweight configuration GreenRFM-L, which can be trained on a *single consumer-grade laptop (6GB VRAM)*, surpasses VoCo. This challenges the prevailing dogma that brute-force scaling is the only path to foundation model performance, demonstrating that *principled MUST supervision design* is an effective, yet less discovered driver of diagnostic capability.

More importantly, on the external RAD-ChestCT dataset, our model achieves an AUC of 78.0%, demonstrating a robust generalization to unseen data distributions. Similarly, on the external Merlin benchmark, we achieve an F1 score of 84.3%, a substantial improvement over the previous state-of-the-art (74.1%) (Table 1).

### Robustness to different prompts

To ensure that these performance gains are robust and not mere artifacts of prompt engineering, we further evaluate our model using five distinct prompts:

- **Prompt 1:** “*{pathology}*.” vs. “*not {pathology}*.”
- **Prompt 2:** “*{pathology}*.” vs. “” (empty string).
- **Prompt 3:** “*There is {pathology}*.” vs. “*There is no {pathology}*.”
- **Prompt 4:** “*{pathology} is present*.” vs. “*{pathology} is not present*.”
- **Prompt 5:** “*Findings are compatible with {pathology}*.” vs. “*Findings are not compatible with {pathology}*.”

Even with the least effective prompt, our model maintains a zero-shot AUC of 82.5% on CT-RATE, a performance that remains on par with the state-of-the-art reported in previous studies. While standard RFMs often exhibit high sensitivity to prompt engineering and require carefully crafted templates, our framework, by anchoring representations to structured diagnostic labels, inherently mitigates this dependency. This “pathology-grounded” alignment ensures that the model captures the underlying pathology rather than overfitting to specific textual patterns, theoretically offering greater stability and reducing the burden of prompt-tuning in clinical deployment.

## Generalization to private clinical benchmarks

To rigorously stress-test our model’s utility in real-world, non-curated clinical environments, we extend our evaluation to two large-scale private datasets collected from our partner institutions: *AH-Chest* and *AH-Abd*. These datasets represent a significant challenge as they contain raw, uncurated clinical data with varying acquisition protocols and significant class imbalances, mirroring the true complexity of daily radiological practice—ranging from high-noise low-dose screening (*AH-Chest*) to thick-slice (5mm vs. 3mm of Merlin) abdominal protocols (*AH-Abd*). Detailed dataset statistics are provided in Supplementary Table [S1](#), [S2](#), and [S3](#).

We evaluate our model’s zero-shot diagnostic performance on these datasets without any fine-tuning. As shown in Table 2, our method demonstrates remarkable robustness, achieving high AUC scores across all three domains. This indicates that the representations learned through our principled supervision framework does not overfit the training distribution (*CT-RATE* and *Merlin*), instead it captures fundamental, transferable features.

**Table 2: Generalization across private benchmarks.** Comparison of zero-shot diagnostic performance on *AH-Chest* and *AH-Abd*.

Method	AH-Chest				AH-Abd			
	AUC	ACC	F1	Prec.	AUC	ACC	F1	Prec.
BrgSA [42]	61.2	74.3	74.9	16.2	-	-	-	-
Merlin [27]	-	-	-	-	60.3	59.9	67.2	23.4
<b>GreenRFM (ours)</b>	<b>74.5</b>	<b>71.3</b>	<b>74.7</b>	<b>40.2</b>	<b>73.2</b>	<b>87.4</b>	<b>85.4</b>	<b>40.3</b>

## Cross-modal retrieval capabilities

Beyond diagnostic classification, we evaluate the semantic alignment of our model through report-to-volume retrieval tasks. This task is particularly challenging as it requires the model to identify the correct CT volume from a large candidate pool based solely on a textual description. As shown in Table 3, our method establishes new benchmarks across all datasets.

On the internal *CT-RATE* dataset (n=3,039), our model achieves a Recall@50 of 39.9% and Recall@100 of 54.3%, significantly outperforming the previous state-of-the-art BrgSA (28.6% and 42.0%) and *CT-CLIP* (18.0% and 28.7%). The performance gap is even more pronounced on the *Merlin* dataset (n=5,082), where our method achieves a Recall@5 of 22.5%, nearly an order of magnitude higher than the *Merlin* baseline (2.9%). This suggests that our supervision strategy, which enforces diagnostic consistency, leads to a much tighter coupling between visual features and their semantic descriptors.

We also extend this evaluation to the large-scale private datasets, *AH-Chest* (n=63,378) and *AH-Abd* (n=14,038). The sheer size of these candidate pools makes retrieval extremely difficult, as evidenced by the near-zero performance of random baselines. Despite this, our model maintains a consistent advantage. On *AH-Abd*, for instance, we achieve a Recall@100 of 6.2%, compared to 2.9% for the *Merlin* model. We observe particularly large gains in Recall@50 and Recall@100, suggesting that our model effectively retrieves relevant cases even from a massive, heterogeneous candidate pool. These results highlight that a principled supervision design can yield a highly performant and robust foundation model without the need for excessive model complexity.

## Extension to MRI modality

To demonstrate the modality-agnostic nature of our framework, we extend our evaluation to MRI datasets (*AH-Knee* and *AH-Spine*) from our partner hospital. Given the absence of large-scale public MRI image-report paired datasets — a well-known bottleneck in the field — we utilize these private datasets for this proof-of-concept validation. To ensure a rigorous

**Table 3: Report-to-volume retrieval performance across datasets.** Comparison of Recall@K metrics on CT-RATE, Merlin, AH-Chest, and AH-Abd. Our method demonstrates superior retrieval capabilities, especially at higher recall thresholds.

Dataset	Method	R@5	R@10	R@50	R@100
CT-RATE (n=3,039)	Random	0.1	0.4	2.0	3.4
	VocabFine [13]	0.1	0.6	2.3	2.0
	CT-CLIP [13]	2.9	5.0	18.0	28.7
	Merlin [27]	1.5	2.7	7.7	12.7
	BrgSA [42]	5.8	10.1	28.6	42.0
	<b>GreenRFM (ours)</b>	<b>9.5</b>	<b>16.0</b>	<b>39.9</b>	<b>54.3</b>
Merlin (n=5,082)	Random	0.1	0.2	1.0	1.8
	Merlin [27]	2.9	4.8	14.6	23.0
	<b>GreenRFM (ours)</b>	<b>22.5</b>	<b>32.9</b>	<b>62.2</b>	<b>74.8</b>
AH-Chest (n=63,378)	Random	0.01	0.01	0.07	0.14
	BrgSA [42]	0.02	0.03	0.12	0.23
	<b>GreenRFM (ours)</b>	<b>0.11</b>	<b>0.21</b>	<b>0.80</b>	<b>1.30</b>
AH-Abd (n=14,038)	Random	0.06	0.09	0.4	0.8
	Merlin [27]	0.22	0.38	1.6	2.9
	<b>GreenRFM (ours)</b>	<b>0.70</b>	<b>1.30</b>	<b>4.0</b>	<b>6.2</b>

and fair comparison, we train a domain-adapted CLIP baseline (denoted as MRCLIP) from scratch on the exact same data split. This baseline employs a specialized vision encoder designed to process multi-plane, multi-sequence MRI inputs, ensuring it can effectively capture the volumetric spatial information. However, unlike our method, it is optimized using the standard contrastive loss without our proposed supervision strategies.

As shown in Table 4, our method consistently outperforms the MRCLIP baseline, confirming that the performance gains stem from our principled supervision design rather than data availability or a specific modality.

**Table 4: Zero-shot diagnostic and cross-modal retrieval performance on MRI datasets.** Comparison between MRCLIP (a domain-adapted CLIP baseline) and our method on AH-Knee and AH-Spine datasets. Both models are trained from scratch on the same private data splits.

Dataset	Method	Zero-shot Classification				Report-to-Volume Retrieval			
		AUC	ACC	F1	Prec.	R@5	R@10	R@50	R@100
AH-Knee (n=372)	MRCLIP	72.9	85.5	83.7	41.7	17.2	28.7	78.2	95.1
	<b>GreenRFM (ours)</b>	<b>79.0</b>	<b>87.3</b>	<b>86.1</b>	<b>46.3</b>	<b>26.1</b>	<b>41.2</b>	<b>84.7</b>	<b>97.6</b>
AH-Spine (n=921)	MRCLIP	70.5	87.8	85.7	35.0	7.2	13.4	42.2	65.1
	<b>GreenRFM (ours)</b>	<b>80.8</b>	<b>89.4</b>	<b>88.5</b>	<b>44.5</b>	<b>10.3</b>	<b>18.3</b>	<b>53.0</b>	<b>72.9</b>

## Discussions

The success of modern deep learning systems lies in the ability to **efficiently scale and utilize** supervisory signals [44]. We emphasize that our advocacy for principled supervision does not negate the importance of scaling; rather, we posit that designing methods to be inherently more data-efficient is the key to unlocking true scalability in medical AI. While the "scale-is-all-you-need" philosophy has driven breakthroughs in general vision, its brute-force application in medicine often hits a ceiling due to data scarcity and noise. Our work demonstrates that by applying principled supervision design, we can amplify the value of training samples, allowing us to build foundation models that are not only performant but also computationally accessible and scalable to larger, more diverse cohorts.

Crucially, our framework delivers not just higher performance, but significantly stronger generalization — a critical attribute often lacking in current foundation models. Recent critiques have highlighted the fragility of medical models trained via generic self-supervised learning, noting their susceptibility to domain shifts and adversarial noise due to a reliance on superficial textural features rather than semantic understanding. By anchoring our model’s representations in structured, clinically meaningful diagnostic labels through ubiquitous supervision, we mitigate this fragility. Our extensive validation across diverse external benchmarks (RAD-ChestCT, AH-Chest, and AH-Abd) and proof-of-concept MRI cohorts (AH-Knee and AH-Spine) demonstrates that this domain-grounded approach yields representations robust to the variations in scanners and protocols, which typically plague clinical deployment.

A key contribution of this work is to distill and unify a set of insights that have often been pursued in isolation. Our framework synthesizes insights from recent advances through the lens of four design principles. For instance, works like Merlin [27] split reports into positive and negative segments to align them separately with evaluation (Task-aligning supervision), while BrgSA [42] and fVLM [33] introduce denser constraints (Ubiquitous Supervision). Similarly, DLILP [21] hints at the importance of discriminative unimodal representation (semantics-enforcing). In contrast, our work systematically distills these insights and integrates them into a unified pipeline.

A common concern is that supervised pre-training might lead the model to overlook rich semantic information in radiology reports — such as lesion size, shape, or texture — that does not directly correspond to predefined labels. We address this by evaluating alignment performance on report sentences that do not contain diagnostic keywords. Our results show that the model maintains high alignment accuracy on these “label-unrelated” descriptions (Fig. 3c). Furthermore, the robust performance in cross-modal retrieval tasks (Table 3) provides additional evidence that the model captures comprehensive semantic information beyond just diagnostic labels. These results indicate that strong diagnostic supervision does not compromise semantic richness. Instead, it appears to provide a robust scaffold upon which fine-grained details are effectively preserved.

Furthermore, our emphasis on “Task-aligning supervision” highlights a common pitfall: the disconnect between pre-training proxies and downstream evaluation protocols. We show that subtle inconsistencies between training stages — such as mismatched feature normalization or pooling strategies — can lead to performance drops of over 2%. Importantly, this degradation often exceeds the gains achieved by adding tens of thousands of training samples.

Finally, our work advocates for “democratized and Green AI” initiative by directly addressing the prohibitive resource intensity of current foundation models. Currently, the field exhibits a dichotomy: industrial giants prioritize aggressive scaling by directly transplanting natural vision paradigms, whereas academic researchers typically concentrate on methodology development within constrained data regimes. However, relying solely on scaling models and computational resources risks restricting progress to a few elite institutions [19]. Scientific advancement, particularly in healthcare, requires democratization and the participation of diverse communities to ensure equitable solutions. Our framework circumvents the dependency on massive compute through principled supervision design, achieving state-of-the-art performance using only 24 GPU hours on a single RTX 3090. This stands in stark contrast to models like VoCo [18] and Pillar-0 [45] that consume tens of thousands of high-performance GPU hours. Moreover, our “Lightweight” version is trainable on consumer-grade laptops (6GB VRAM). This capability is transformative: it empowers clinicians to train customized models directly on hospital hardware, ensuring data privacy and adaptation to local demographics without requiring high-performance computing infrastructure. Such efficiency also reduces the carbon footprint (estimated CO<sub>2</sub>e) by orders of magnitude. By substituting raw computational scale with high-quality supervision, we offer a sustainable,

democratized path for medical AI development.

We acknowledge that our study is limited by its retrospective nature and the lack of large-scale human verification of the LLM-extracted labels. This raises a critical question: does the model’s performance stem from genuine clinical understanding or merely from “label engineering”—overfitting to the systematic biases of the LLM generator? Our results provide three lines of evidence against the latter. First, we validate the LLM labels against human-verified ground truth (Merlin), achieving high agreement on definitive findings, the result is consistent with our preliminary results [20] and other prior work [28]. Second, for private datasets, we employ a dual-LLM consensus protocol to filter out model-specific hallucinations. Third, and most importantly, our framework generalizes robustly to external benchmarks (e.g., RAD-ChestCT, AH-Knee and AH-Spine) with independent, human-curated labeling protocols. This successful transfer confirms that our principled supervision captures intrinsic pathological features rather than annotation artifacts. Furthermore, the observed robustness to label noise [30] suggests that the lack of perfect ground truth does not undermine the model’s fundamental capabilities. Future work should extend this validation to prospective multi-center trials. Ultimately, this work provides a blueprint for the next generation of radiology foundation models: models that are not just “trained on more data,” but are “trained better” through principled, clinically aligned supervision.

## Methods

### Overview of the principled supervision design framework

**Problem Setup.** Let  $\mathcal{X} \subset \mathbb{R}^{H \times W \times D}$  denote the domain of 3D medical volumes and  $\mathcal{R}$  denote the space of unstructured textual reports. Given a dataset  $\mathcal{D} = \{(x_i, r_i)\}_{i=1}^N$  of paired 3D medical images  $x_i \in \mathcal{X}$  and corresponding unstructured reports  $r_i \in \mathcal{R}$ , our goal is to develop radiology foundation models (RFMs) [19] that align visual and textual representations via large-scale pre-training. In particular, we aim to capture radiology findings and clinically relevant concepts to support diverse multimodal downstream tasks, such as natural-language-based diagnosis and cross-modal retrieval. The training process should avoid reliance on human-provided labels.

Guided by the four design philosophies outlined in the Introduction, we propose a Principled Supervision Design Framework for building performant RFMs. Our framework operationalizes these principles into a cohesive pipeline: (1) **More distilled supervision:** We leverage LLMs to distill unstructured reports into scalable, structured diagnostic labels. (2) **Task-aligning supervision:** We meticulously align the architectural design (e.g., pooling, normalization) and domain choices (e.g., text encoder) with downstream diagnostic protocols. (3) **Ubiquitous supervision & Semantics-enforcing supervision:** We employ a two-stage training strategy that injects supervision into every component—vision encoder, text encoder, and alignment space—ensuring discriminative representations are matured before alignment.

### More distilled supervision via LLM-powered label extraction

To achieve more distilled supervision, we generate high-quality supervisory signals without manual annotation. We design a simple yet effective prompt template for LLMs to extract abnormality labels from radiology reports. The system prompt clearly defines each category and enforces a strict output format (18 or 30 comma-separated integers), instructing the LLM to classify the status of specific conditions as present (1), absent (0), or uncertain/missing (-1).

Crucially, to handle real-world clinical ambiguity, we explicitly model missing or uncertain labels. This process converts unstructured free text into dense, structured supervisory signals that drive the subsequent stages. We find the LLMs may fail to adhere to the output format

in some cases, for example, when the report writes “nodule in both Lungs” it may output a number of “2” instead of “1” for the “Nodule” category. To ensure robustness, we perform automatic output verification (post-processing) on the LLM response. The verifier checks that the response is exactly 18 or 30 comma-separated tokens and that each token is one of {"1","0","-1"}. If the check fails we treat the output as invalid and re-query it until a maximum number of attempts is met, after which we flag the instance for manual review.

### Task-aligning supervision

To ensure that the pre-trained model translates seamlessly to downstream diagnostic tasks, we enforce *Task-Aligning supervision* across four key architectural and design dimensions.

**Domain consistency (text encoder).** We select CXR-BERT [34] over generic clinical language models to maintain domain consistency. Unlike general biomedical models, CXR-BERT is pre-trained specifically on radiology reports with a specialized tokenizer, ensuring that the semantic space is rooted in radiology terminology rather than general medical literature.

**Consistency in supervision goal (diagnostic labels).** We prioritize diagnostic labels over generic visual descriptions to ensure the pre-training objective is strictly aligned with the downstream diagnostic task. While visual descriptions (e.g., texture, shape) capture morphological details, they do not directly map to clinical decisions. By supervising the model with explicit diagnostic concepts (e.g., “Pneumonia”, “Mass”), we force the encoder to learn features that are causally linked to pathology, minimizing the gap between the pre-training proxy task and the final diagnostic application.

**Architectural consistency (vision encoder & pooling).** We employ a 3D ResNet-18 (initialized with Kinetics-400 weights [46]) as our vision encoder  $f_I$ . We offer two configurations to balance performance and resource efficiency. For the resource-efficient “Lite” version, we modify the initial stem convolution to use a kernel size and stride of (4, 4, 4), which aggressively downsamples the input volume to reduce computational overhead and memory usage. Crucially, to ensure consistency with alignment stage and downstream zero-shot evaluation which typically operates on global volume representations, we utilize Global Average Pooling (GAP) to aggregate the 3D feature maps into a vector  $z \in \mathbb{R}^c$ :

$$z = \text{GAP}(F) = \frac{1}{D'H'W'} \sum_{d,h,w} F_{d,h,w}. \quad (1)$$

This design choice mitigates performance degradation stemming from the structural discrepancy between training and inference protocols.

**Consistency in feature geometry (no  $L_2$  normalization).** Standard CLIP training enforces  $L_2$  normalization, projecting features onto a hypersphere. However, diagnostic confidence is often encoded in feature magnitude. Enforcing  $L_2$  normalization during alignment would obliterate this learned confidence signal. To maintain consistency between pre-training and inference, we remove the  $L_2$  normalization constraint in the contrastive loss calculation, allowing the model to preserve the semantic magnitude.

$$\text{sim}(z, t) = z^\top t = \|z\| \|t\| \cos \theta, \quad (2)$$

where  $z$  and  $t$  represent the image and text embeddings, respectively. Unlike standard cosine similarity which only captures angular distance ( $\cos \theta$ ), this formulation allows the embedding norm to preserve the confidence or severity learned in supervised pre-training.

**Consistency in semantic focus (shared classifier).** To ensure that the cross-modal alignment serves the ultimate goal of diagnosis, we introduce a shared linear classifier that operates on both the projected image and text embeddings. This anchors the alignment space to high-level pathological concepts rather than superficial visual-textual correlations.

## Ubiquitous supervision and semantics-enforcing supervision (training strategy)

We implement the above designs within a two-stage training strategy that prioritizes *semantics-enforcing* and applies *ubiquitous supervision*.

**Stage 1: Supervised pre-training.** We first mature the encoders independently to ensure they learn discriminative features.

- **Vision encoder:** The encoder is supervised by the shared linear classifier predicting the diagnostic labels via Binary Cross Entropy (BCE) loss ( $\mathcal{L}_{\text{BCE}}$ ). Additionally, when anatomical segmentation masks are available (e.g., for CT datasets), we attach a lightweight decoder to predict coarse anatomical segmentation masks  $M$  [47] (derived from totalSegmentator [48]), optimized via Cross-Entropy loss ( $\mathcal{L}_{\text{seg}}$ ). The total vision loss is  $\mathcal{L}_{\text{vision}} = \mathcal{L}_{\text{BCE}} + \mathcal{L}_{\text{seg}}$ .
- **Text encoder:** We apply ubiquitous supervision by attaching a classification head to the ‘[CLS]’ token embedding of the text encoder. This forces the text encoder to extract explicit diagnostic signals, optimizing  $\mathcal{L}_{\text{text}}$  via BCE.

**Stage 2: Contrastive alignment.** In the second stage, we align the matured encoders. We optimize a joint objective combining the contrastive loss (without  $L_2$  normalization) and the shared classifier loss. The contrastive loss is defined as:

$$\mathcal{L}_{\text{CLIP}} = -\frac{1}{2N} \sum_{i=1}^N \left[ \log \frac{\exp(z_i^\top t_i)}{\sum_{j=1}^N \exp(z_i^\top t_j)} + \log \frac{\exp(z_i^\top t_i)}{\sum_{j=1}^N \exp(z_j^\top t_i)} \right]. \quad (3)$$

The total objective is:

$$\mathcal{L}_{\text{total}} = \mathcal{L}_{\text{CLIP}} + \lambda(\mathcal{L}_{\text{cls\_img}} + \mathcal{L}_{\text{cls\_txt}}) \quad (4)$$

where  $\mathcal{L}_{\text{CLIP}}$  is the standard contrastive loss computed on non-normalized embeddings, and  $L_{\text{cls}}$  ensures that both image and text embeddings remain discriminative for the diagnostic labels throughout the alignment process.

**Implementation details.** We use the AdamW optimizer with a learning rate of  $1 \times 10^{-4}$  for supervised pre-training of the image encoder,  $1 \times 10^{-5}$  for supervised pre-training of the text encoder, and  $1 \times 10^{-5}$  for cross modal alignment. The batch size was set to 10 for both stages and for both CT-RATE and Merlin, and positive/negative samples are weighted equally in the BCE loss.

## Ethics approval

Our retrospective study in this investigation is approved by the Institutional Review Board (IRB) of the hospitals with a waiver granted for the requirement of informed consent.

## Datasets

In total, our study involves 111,130 scans corresponding to 200,453 images across diverse modalities and anatomies. We utilize two large-scale public CT datasets for training.

**CT-RATE** [13] serves as our internal training and validation set, containing 50,188 reconstructed volumes from 25,692 scans of 21,304 patients. It includes radiology reports and 18 abnormality labels extracted via a BERT-based tool. We strictly follow the official training/validation splits.

**Merlin** [27] is a high-quality abdominal CT dataset from Stanford University Medical Center, containing 25,528 scans from 18,321 patients. It provides labels for 30 abnormalities, including explicit markers for missing or uncertain findings. We report results on the official internal test set (5,137 scans).

We use **RAD-ChestCT** [49] and two private CT datasets (**AH-Chest** and **AH- Abd**) as external validation sets.

The **RAD-ChestCT** dataset comprises 36,316 non-contrast chest CTs from Duke University (2012-2017). We utilize the public available subset of 3,630 scans to test generalization to unseen distributions.

**AH-Chest** and **AH-Abd** are plain chest CT and contrast-enhanced abdominal CT scans collected from The First Affiliated hospital of University of Science and Technology of China (AnHui Provincial Hospital) between August 2021 and June 2023, containing 29,377 and 14,038 scans respectively. The AH-Chest contains 63,378 reconstructed images. The plain chest CT scans usually contain 1 ~ 3 images, with raw data reconstructed into different slice thickness (0.625mm, 5mm) or different reconstruction kernels (sharp kernel, smooth kernel). We keep all the reconstructed images for experiments. The contrast-enhanced abdominal CT scans usually contain a plain phase and a contrast-enhanced phase, with many containing more than one contrast-enhanced phase. For examination with only two phases, we select the contrast-enhanced phase for experiments. For examination with more than two phases, we select the portal venous phase for experiments if available; otherwise, we select the arterial phase. All scans are de-identified before processing and analysis.

**AH-Knee** and **AH-Spine** are musculoskeletal MRI datasets concurrently acquired from the same institution. **AH-Knee** comprises 3,662 studies (15,431 images) focusing on knee pathologies, while **AH-Spine** includes 9,203 studies (28,260 images) targeting spinal conditions. Each examination typically consists of multi-sequence (PD, T1, T2) and multi-planar (Sagittal, Coronal, Transverse) acquisitions, though specific sequences or planes may be absent in some cases. For both datasets, we employ the identical LLM-driven pipeline to extract diagnostic labels from the corresponding radiology reports.

### Data preprocessing

For **CT-RATE**, **RAD-ChestCT** and **AH-Chest**, all chest CT volumes are resampled to an in-plane spacing of 1.5 mm  $\times$  1.5 mm and slice thickness of 3.0 mm via trilinear interpolation. Hounsfield Units are clipped to a lung-relevant window ([-1000, 200] HU) and linearly normalized to the range [-1, 1]. Volumes are first padded or cropped to a fixed canvas of 240  $\times$  240  $\times$  120 voxels, then randomly cropped to 192  $\times$  192  $\times$  96 during training. At evaluation time, we use a single center crop of size 192  $\times$  192  $\times$  96.

For the abdominal **Merlin** dataset, we adopt a similar pipeline but with abdomen-appropriate settings. Volumes are resampled to 1.5 mm  $\times$  1.5 mm  $\times$  3.0 mm, intensities are clipped to a wider range ([-1000, 1000] HU) and normalized to [-1, 1]. Each volume is padded/cropped to 280  $\times$  280  $\times$  180, followed by random crops of 224  $\times$  224  $\times$  144 for training and a center crop of the same size for evaluation.

For AH-Abd, as the images in AnHui Provincial Hospital are mostly reconstructed with 5mm slice thickness, we resample the volumes to an in-plane spacing of 1.5 mm  $\times$  1.5 mm and slice thickness of 5.0 mm. The other preprocessing steps are the same as in the Merlin dataset. We remove the CT scans with a slice number less than 50.

For the MRI datasets (**AH-Knee** and **AH-Spine**), we adopt a multi-view multi-sequence preprocessing pipeline. We group images by plane (Sagittal, Coronal, Transverse) and sequence (PD, T1, T2). Images within the same plane are resampled to match the spacing of the PD sequence. We compute a joint bounding box using Otsu thresholding and crop the volumes with a margin. Intensity values are normalized using Z-score normalization based on foreground voxels. Finally, the images are padded to a fixed size and resized to 240  $\times$  240  $\times$  24. During training, we apply random cropping of size 192  $\times$  192  $\times$  20.

For AH-Chest and AH-Abd, we use the same LLM-powered label extraction pipeline to obtain abnormality labels from the corresponding radiology reports. We extract 18 abnormality labels for AH-Chest and 30 abnormality labels for AH-Abd, which is consistent with CT-RATE and Merlin datasets respectively. We use Qwen [50] and Doubao [51] LLMs to

extract labels for AH-Chest and AH-Abd, and use the categories only when an agreement rate between the two LLMs is greater than 90%. We also consult with the collaborating radiologists from AnHui Provincial Hospital to determine the appropriate abnormality categories for these datasets, as some categories, such as ‘‘Mosaic Attenuation Pattern’’, exist in CT-RATE but are not commonly reported in AnHui Provincial Hospital.

For the MRI datasets (AH-Knee and AH-Spine), we similarly employ the LLM-driven label extraction pipeline to derive diagnostic labels from radiology reports. For AH-Knee, we extract 13 abnormality labels focusing on common knee abnormalities such as meniscal tears and ligament injuries. For AH-Spine, we identify 8 abnormality labels related to spinal conditions including disc herniation, spinal stenosis, and vertebral fractures. The selection of these categories is informed by consultations with musculoskeletal radiologists to ensure clinical relevance. We split the MRI dataset into a ratio of 9:1 for training and validation, and we manually review the labels in the validation set given their relatively small size. Different from the CT datasets, the MRI examinations usually have a high portion of positive findings. As the report usually contains detailed descriptions of the findings, especially for musculoskeletal systems, we do not include the uncertain/missing label (-1) in the MRI datasets.

### Evaluation metrics

We utilize a diverse set of metrics to comprehensively evaluate the performance of our framework.

For **Diagnostic Label Quality**, we assess the agreement between LLM-generated labels and human annotations using Cohen’s Kappa ( $\kappa$ ), Accuracy, Precision, Recall, and F1-score.

For **Zero-shot Diagnosis**, we report the Area Under the Curve (AUC), Accuracy, F1-score, Precision, Sensitivity, and Specificity. For each disease  $c$ , we use a positive prompt  $T_c^+$  (e.g., ‘‘disease name’’) and a negative prompt  $T_c^-$  (e.g., ‘‘no disease name’’). Given an image  $I$  with embedding  $v = f_I(I)$  and text embeddings  $t_c^+ = f_T(T_c^+)$ ,  $t_c^- = f_T(T_c^-)$ , the disease probability is obtained by a softmax over the similarities:

$$P(c | I) = \frac{\exp(\text{sim}(v, t_c^+))}{\exp(\text{sim}(v, t_c^+)) + \exp(\text{sim}(v, t_c^-))}, \quad (5)$$

where  $\text{sim}(v, t) = v^\top t$  denotes the dot-product similarity.

For **Report-to-Image Retrieval**, we embed each report  $T_i$  into  $t_i = f_T(T_i)$  and rank all images  $I_j$  in the test set by similarity  $\text{sim}(t_i, v_j)$ . We evaluate performance using Recall@ $k$  for  $k \in \{1, 5, 10, 50, 100\}$ , which measures the proportion of reports for which the correct paired image appears within the top- $k$  retrieved candidates.

### Grad-CAM visualization

To qualitatively interpret the prediction of the model, we employ Gradient-weighted Class Activation Mapping (Grad-CAM [52]). Given an input volume  $I$  and a target diagnostic prompt  $T$  describing a specific pathology (e.g., ‘‘There is pathology.’’), we compute the similarity score  $S = \text{sim}(f_I(I), f_T(T))$ . We then backpropagate the gradients of this score with respect to the feature maps  $A^k$  of the last convolutional layer (layer4) of the 3D ResNet-18 image encoder. The importance weights  $\alpha_k$  for each feature map  $k$  are obtained by global average pooling of the gradients:

$$\alpha_k = \frac{1}{Z} \sum_i \sum_j \sum_l \frac{\partial S}{\partial A_{ijl}^k}, \quad (6)$$

where  $Z$  is the number of elements in the feature map. The localization map  $L_{\text{Grad-CAM}}$  is then computed as a weighted combination of the feature maps, followed by a ReLU activation

to isolate features that have a positive influence on the target class:

$$L_{\text{Grad-CAM}} = \text{ReLU} \left( \sum_k \alpha_k A^k \right). \quad (7)$$

Finally, the resulting low-resolution heatmap is upsampled via trilinear interpolation to the original input resolution and overlaid on the CT or MRI volume for visualization. This allows us to inspect whether the model’s attention aligns with clinically significant regions identified by radiologists. Visualization of heatmap is provided in Fig. S3 and Fig. S4.

## Data availability

The CT-RATE dataset is available at <https://huggingface.co/datasets/ibrahimhamamci/CT-RATE>. The RAD-ChestCT dataset is available at <https://zenodo.org/records/6406114>. The Merlin dataset is available at <https://stanfordaimi.azurewebsites.net/datasets/60b9c7ff-877b-48ce-96c3-0194c8205c40>. The private datasets (AH-Chest, AH-Abd, AH-Knee and AH-Spine) are not publicly available due to patient privacy restrictions but may be available from the corresponding author upon reasonable request and institutional approval.

## Code availability

The code is available on Github at <https://github.com/SadVoxel/GreenRFM>.

## References

- [1] Diego Ardila, Atilla P Kiraly, Sujeeth Bharadwaj, Bokyung Choi, Joshua J Reicher, Lily Peng, Daniel Tse, Mozziyar Etemadi, Wenxing Ye, Greg Corrado, et al. End-to-end lung cancer screening with three-dimensional deep learning on low-dose chest computed tomography. *Nature medicine*, 25(6):954–961, 2019.
- [2] Kai Cao, Yingda Xia, Jiawen Yao, Xu Han, Lukas Lambert, Tingting Zhang, Wei Tang, Gang Jin, Hui Jiang, Xu Fang, et al. Large-scale pancreatic cancer detection via non-contrast ct and deep learning. *Nature medicine*, 29(12):3033–3043, 2023.
- [3] Yujian Hu, Yilang Xiang, Yan-Jie Zhou, Yangyan He, Dehai Lang, Shifeng Yang, Xiaolong Du, Chunlan Den, Youyao Xu, Gaofeng Wang, et al. Ai-based diagnosis of acute aortic syndrome from noncontrast ct. *Nature Medicine*, pages 1–13, 2025.
- [4] Yan-Ran Wang, Kai Yang, Yi Wen, Pengcheng Wang, Yuepeng Hu, Yongfan Lai, Yufeng Wang, Kankan Zhao, Siyi Tang, Angela Zhang, et al. Screening and diagnosis of cardiovascular disease using artificial intelligence-enabled cardiac magnetic resonance imaging. *Nature Medicine*, pages 1–10, 2024.
- [5] Sebastiaan Hermans, Zixuan Hu, Robyn L Ball, Hui Ming Lin, Luciano M Prevedello, Ferco H Berger, Ibrahim Yusuf, Jeffrey D Rudie, Maryam Vazirabad, Adam E Flanders, et al. Rsnai 2023 abdominal trauma ai challenge: Review and outcomes. *Radiology: Artificial Intelligence*, 7(1):e240334, 2024.
- [6] Kaiming Dong, Yuxiao Cheng, Kunlun He, and Jinli Suo. A generative model uses healthy and diseased image pairs for pixel-level chest x-ray pathology localization. *Nature Biomedical Engineering*, pages 1–13, 2025.
- [7] Christian Bluethgen, Pierre Chambon, Jean-Benoit Delbrouck, Rogier Van Der Sluijs, Małgorzata Polacin, Juan Manuel Zambrano Chaves, Tanishq Mathew Abraham, Shivanshu Purohit, Curtis P Langlotz, and Akshay S Chaudhari. A vision–language foundation model for the generation of realistic chest x-ray images. *Nature Biomedical Engineering*, 9(4):494–506, 2025.
- [8] Robin Rombach, Andreas Blattmann, Dominik Lorenz, Patrick Esser, and Björn Ommer. High-resolution image synthesis with latent diffusion models. In *Proceedings of the IEEE/CVF conference on computer vision and pattern recognition*, pages 10684–10695, 2022.

- [9] Jean-Baptiste Alayrac, Jeff Donahue, Pauline Luc, Antoine Miech, Iain Barr, Yana Hasson, Karel Lenc, Arthur Mensch, Katherine Millican, Malcolm Reynolds, et al. Flamingo: a visual language model for few-shot learning. *Advances in neural information processing systems*, 35:23716–23736, 2022.
- [10] Junnan Li, Dongxu Li, Silvio Savarese, and Steven Hoi. Blip-2: Bootstrapping language-image pre-training with frozen image encoders and large language models. In *International conference on machine learning*, pages 19730–19742. PMLR, 2023.
- [11] Haotian Liu, Chunyuan Li, Qingyang Wu, and Yong Jae Lee. Visual instruction tuning. *Advances in neural information processing systems*, 36:34892–34916, 2023.
- [12] Cameron Beeche, Joonghyun Kim, Hamed Tavolinejad, Bingxin Zhao, Rakesh Sharma, Jeffrey Duda, James Gee, Farouk Dako, Anurag Verma, Colleen Morse, et al. A pan-organ vision-language model for generalizable 3d ct representations. *medRxiv*, 2025.
- [13] Ibrahim Ethem Hamamci, Sezgin Er, Furkan Almas, Ayse Gulnihan Simsek, Seval Nil Esirgun, Irem Dogan, Muhammed Furkan Dasdelen, Bastian Wittmann, Enis Simsar, Mehmet Simsar, et al. A foundation model utilizing chest ct volumes and radiology reports for supervised-level zero-shot detection of abnormalities. *CoRR*, 2024.
- [14] Rongsheng Wang, Fenghe Tang, Qingsong Yao, Rui Yan, Xu Zhang, Zhen Huang, Haoran Lai, Zhiyang He, Xiaodong Tao, Zihang Jiang, et al. Simcrop: Radiograph representation learning with similarity-driven cross-granularity pre-training. In *International Conference on Medical Image Computing and Computer-Assisted Intervention*, pages 563–573. Springer, 2025.
- [15] Alec Radford, Jong Wook Kim, Chris Hallacy, Aditya Ramesh, Gabriel Goh, Sandhini Agarwal, Girish Sastry, Amanda Askell, Pamela Mishkin, Jack Clark, et al. Learning transferable visual models from natural language supervision. In *International conference on machine learning*, pages 8748–8763. PmLR, 2021.
- [16] Hamid R Tizhoosh. Beyond the failures: Rethinking foundation models in pathology. *arXiv preprint arXiv:2510.23807*, 2025.
- [17] Zhihong Chen, Yuhao Du, Jinpeng Hu, Yang Liu, Guanbin Li, Xiang Wan, and Tsung-Hui Chang. Multi-modal masked autoencoders for medical vision-and-language pre-training. In Linwei Wang, Qi Dou, P. Thomas Fletcher, Stefanie Speidel, and Shuo Li, editors, *Medical Image Computing and Computer Assisted Intervention – MICCAI 2022*, pages 679–689, Cham, 2022. Springer Nature Switzerland.
- [18] Linshan Wu, Jiaxin Zhuang, and Hao Chen. Large-scale 3d medical image pre-training with geometric context priors. *IEEE Transactions on Pattern Analysis and Machine Intelligence*, 2025.
- [19] Magdalini Paschali, Zhihong Chen, Louis Blankemeier, Maya Varma, Alaa Youssef, Christian Bluethgen, Curtis Langlotz, Sergios Gatidis, and Akshay Chaudhari. Foundation models in radiology: What, how, why, and why not. *Radiology*, 314(2):e240597, 2025.
- [20] Yingtai Li, Haoran Lai, Xiaoqian Zhou, Shuai Ming, Wenxin Ma, Wei Wei, and Shaohua Kevin Zhou. More performant and scalable: Rethinking contrastive vision-language pre-training of radiology in the llm era. In *International Conference on Medical Image Computing and Computer-Assisted Intervention*, pages 348–357. Springer, 2025.
- [21] Julio Silva-Rodríguez, Jose Dolz, and Ismail Ben Ayed. A reality check of vision-language pre-training in radiology: Have we progressed using text? In *International Conference on Information Processing in Medical Imaging*, pages 294–309. Springer, 2025.
- [22] Yuhao Zhang, Hang Jiang, Yasuhide Miura, Christopher D Manning, and Curtis P Langlotz. Contrastive learning of medical visual representations from paired images and text. In *Machine learning for healthcare conference*, pages 2–25. PMLR, 2022.
- [23] Tianhe Yu, Saurabh Kumar, Abhishek Gupta, Sergey Levine, Karol Hausman, and Chelsea Finn. Gradient surgery for multi-task learning. *Advances in neural information processing systems*, 33:5824–5836, 2020.

- [24] Aviv Navon, Aviv Shamsian, Idan Achituve, Haggai Maron, Kenji Kawaguchi, Gal Chechik, and Ethan Fetaya. Multi-task learning as a bargaining game. *arXiv preprint arXiv:2202.01017*, 2022.
- [25] Qiang Meng, Shichao Zhao, Zhida Huang, and Feng Zhou. Magface: A universal representation for face recognition and quality assessment. In *Proceedings of the IEEE/CVF Conference on Computer Vision and Pattern Recognition*, pages 14225–14234, 2021.
- [26] Feng Wang, Xiang Xiang, Jian Cheng, and Alan L Yuille. Normface: L2 hypersphere embedding for face verification. In *Proceedings of the 25th ACM international conference on Multimedia*, pages 1041–1049, 2017.
- [27] Louis Blankemeier, Joseph Paul Cohen, Ashwin Kumar, Dave Van Veen, Syed Jamal Safdar Gardezi, Magdalini Paschali, Zhihong Chen, Jean-Benoit Delbrouck, Eduardo Reis, Cesar Truys, et al. Merlin: A vision language foundation model for 3d computed tomography. *Research Square*, pages rs–3, 2024.
- [28] Hanna Kreutzer, Anne-Sophie Caselitz, Thomas Dratsch, Daniel Pinto dos Santos, Christiane Kuhl, Daniel Truhn, and Sven Nebelung. Large language model-based uncertainty-adjusted label extraction for artificial intelligence model development in upper extremity radiography. *European Radiology*, pages 1–12, 2025.
- [29] Jeremy Irvin, Pranav Rajpurkar, Michael Ko, Yifan Yu, Silvana Ciurea-Ilcus, Chris Chute, Henrik Marklund, Behzad Haghgoo, Robyn Ball, Katie Shpanskaya, et al. Chexpert: A large chest radiograph dataset with uncertainty labels and expert comparison. In *Proceedings of the AAAI conference on artificial intelligence*, volume 33, pages 590–597, 2019.
- [30] David Rolnick, Andreas Veit, Serge Belongie, and Nir Shavit. Deep learning is robust to massive label noise. *arXiv preprint arXiv:1705.10694*, 2017.
- [31] Nathalie Japkowicz and Shaju Stephen. The class imbalance problem: A systematic study. *Intelligent data analysis*, 6(5):429–449, 2002.
- [32] Mateusz Buda, Atsuto Maki, and Maciej A Mazurowski. A systematic study of the class imbalance problem in convolutional neural networks. *Neural networks*, 106:249–259, 2018.
- [33] Zhongyi Shui, Jianpeng Zhang, Weiwei Cao, Sinuo Wang, Ruizhe Guo, Le Lu, Ling Zhang, Tingbo Liang, Lin Yang, Xianghua Ye, and Qi Zhang. Large-scale and fine-grained vision-language pre-training for enhanced ct image understanding. In *The Thirteenth International Conference on Learning Representations*, 2025.
- [34] Benedikt Boecking, Naoto Usuyama, Shruthi Bannur, Daniel C Castro, Anton Schwaighofer, Stephanie Hyland, Maria Wetscherek, Tristan Naumann, Aditya Nori, Javier Alvarez-Valle, et al. Making the most of text semantics to improve biomedical vision–language processing. In *European conference on computer vision*, pages 1–21. Springer, 2022.
- [35] Gabriel Ilharco, Mitchell Wortsman, Nicholas Carlini, Rohan Taori, Achal Dave, Vaishaal Shankar, Hongseok Namkoong, John Miller, Hannaneh Hajishirzi, Ali Farhadi, et al. Openclip. *Zenodo*, 2021.
- [36] Sheng Zhang, Yanbo Xu, Naoto Usuyama, Hanwen Xu, Jaspreet Bagga, Robert Tinn, Sam Preston, Rajesh Rao, Mu Wei, Naveen Valluri, et al. A multimodal biomedical foundation model trained from fifteen million image–text pairs. *NEJM AI*, 2(1):AIoa2400640, 2025.
- [37] Gorkem Can Ates, Yu Xin, Kuang Gong, and Wei Shao. Dformer: Efficient 3d vision-language modeling with decomposed convolutions. *arXiv preprint arXiv:2502.05091*, 2025.
- [38] Jianzhong You, Yuan Gao, Sangwook Kim, and Chris Mcintosh. X2ct-clip: Enable multi-abnormality detection in computed tomography from chest radiography via tri-modal contrastive learning. *arXiv preprint arXiv:2503.02162*, 2025.
- [39] Weiwei Cao, Jianpeng Zhang, Yingda Xia, Tony CW Mok, Zi Li, Xianghua Ye, Le Lu, Jian Zheng, Yuxing Tang, and Ling Zhang. Bootstrapping chest ct image understanding by distilling knowledge from x-ray expert models. In *Proceedings of the IEEE/CVF Conference on Computer Vision and Pattern Recognition*, pages 11238–11247, 2024.

- [40] Chenhui Zhao, Yiwei Lyu, Asadur Chowdury, Edward Harake, Akhil Kondepudi, Akshay Rao, Xinhai Hou, Honglak Lee, and Todd Hollon. Towards scalable language-image pre-training for 3d medical imaging. *arXiv preprint arXiv:2505.21862*, 2025.
- [41] Weiwei Cao, Jianpeng Zhang, Zhongyi Shui, Sinuo Wang, Zeli Chen, Xi Li, Le Lu, Xianghua Ye, Qi Zhang, Tingbo Liang, et al. Boosting vision semantic density with anatomy normality modeling for medical vision-language pre-training. In *Proceedings of the IEEE/CVF International Conference on Computer Vision*, pages 23041–23050, 2025.
- [42] Haoran Lai, Zihang Jiang, Qingsong Yao, Rongsheng Wang, Zhiyang He, Xiaodong Tao, Wei Wei, Weifu Lv, and S Kevin Zhou. Bridged semantic alignment for zero-shot 3d medical image diagnosis. *arXiv preprint arXiv:2501.03565*, 2025.
- [43] Hao-Chih Lee, Zelong Liu, Hamza Ahmed, Spencer Kim, Sean Huver, Vishwesh Nath, Zahi A Fayad, Timothy Deyer, and Xueyan Mei. Unified supervision for vision-language modeling in 3d computed tomography. In *Proceedings of the IEEE/CVF International Conference on Computer Vision*, pages 6725–6733, 2025.
- [44] Rishi Bommasani. On the opportunities and risks of foundation models. *arXiv preprint arXiv:2108.07258*, 2021.
- [45] Kumar Krishna Agrawal, Longchao Liu, Long Lian, Michael Necessian, Natalia Harguindeguy, Yufu Wu, Peter Mikhael, Gigin Lin, Lecia V Sequist, Florian Fintelmann, et al. Pillar-0: A new frontier for radiology foundation models. *arXiv preprint arXiv:2511.17803*, 2025.
- [46] Will Kay, Joao Carreira, Karen Simonyan, Brian Zhang, Chloe Hillier, Sudheendra Vijayanarasimhan, Fabio Viola, Tim Green, Trevor Back, Paul Natsev, et al. The kinetics human action video dataset. *arXiv preprint arXiv:1705.06950*, 2017.
- [47] Yingtai Li, Shuai Ming, Haoran Lai, Fenghe Tang, Wei Wei, and S Kevin Zhou. Scaling supervision for free: Leveraging universal segmentation models for enhanced medical image diagnosis. In *Submitted to Medical Imaging with Deep Learning*, 2025. under review.
- [48] Jakob Wasserthal, Hanns-Christian Breit, Manfred T Meyer, Maurice Pradella, Daniel Hinck, Alexander W Sauter, Tobias Heye, Daniel T Boll, Joshy Cyriac, Shan Yang, et al. Totalsegmentator: robust segmentation of 104 anatomic structures in ct images. *Radiology: Artificial Intelligence*, 5(5):e230024, 2023.
- [49] Rachel Lea Draelos, David Dov, Maciej A Mazurowski, Joseph Y Lo, Ricardo Henao, Geoffrey D Rubin, and Lawrence Carin. Machine-learning-based multiple abnormality prediction with large-scale chest computed tomography volumes. *Medical image analysis*, 67:101857, 2021.
- [50] Jinze Bai, Shuai Bai, Yunfei Chu, Zeyu Cui, Kai Dang, Xiaodong Deng, Yang Fan, Wenbin Ge, Yu Han, Fei Huang, et al. Qwen technical report. *arXiv preprint arXiv:2309.16609*, 2023.
- [51] ByteDance. Doubao: A large language model by bytedance. <https://www.doubao.com>, 2023. Accessed: June 2024.
- [52] Ramprasaath R Selvaraju, Michael Cogswell, Abhishek Das, Ramakrishna Vedantam, Devi Parikh, and Dhruv Batra. Grad-cam: Visual explanations from deep networks via gradient-based localization. In *Proceedings of the IEEE international conference on computer vision*, pages 618–626, 2017.

## Appendix

### A. Demographic statistics of datasets

We utilize five large-scale datasets in this study: CT-RATE, Merlin, RAD-ChestCT, AH-Chest, and AH-Abd. The demographic details, including the number of scans, patients, age distribution, and sex distribution, are summarized in Table S1.

**Table S1: Demographic statistics of the five datasets.** Note: M = Male, F = Female. Values are presented as Mean  $\pm$  Std or Count (%).

Dataset	Modality	# Scans	# Patients	Age (Years)	Sex (M/F)
CT-RATE (Train/Val)	Chest CT	25,692	21,304	-	29238/20944
Merlin (Train/Val)	Abd CT	25,528	18,321	53.8 $\pm$ 19.5	10254/8065
RAD-ChestCT (Ext. Val)	Chest CT	3,630	-	-	-
AH-Chest (Private)	Chest CT	29,377	-	51.6 $\pm$ 16.3	15160/14216
AH-Abd (Private)	Abd CT	14,038	-	58.6 $\pm$ 13.5	7575/6463
AH-Knee (Private)	Knee MRI	3,662	-	45.3 $\pm$ 18.3	1461/2201
AH-Spine (Private)	Spine MRI	9,203	-	51.3 $\pm$ 17.3	3847/5356

### B. Label distribution analysis

The distribution of abnormality labels varies significantly across the datasets, reflecting different clinical populations and acquisition protocols. Table S2 and Table S3 illustrate the prevalence of each pathology in the respective datasets.

**Table S2: Label distribution for AH-Chest dataset.** The dataset contains 29,377 samples in total. The counts and percentages for Uncertain/missing (-1), Negative (0), and Positive (1) labels are shown.

Label	Uncertain/missing (-1)	Negative (0)	Positive (1)
Medical Material	19349 (65.86%)	6709 (22.84%)	3319 (11.30%)
Arterial Wall Calcification	25351 (86.30%)	3174 (10.80%)	852 ( 2.90%)
Cardiomegaly	22832 (77.72%)	5749 (19.57%)	796 ( 2.71%)
Pericardial Effusion	24896 (84.75%)	3463 (11.79%)	1018 ( 3.47%)
Coronary Artery Wall Calcification	25797 (87.81%)	2956 (10.06%)	624 ( 2.12%)
Hiatal Hernia	27091 (92.22%)	2183 ( 7.43%)	103 ( 0.35%)
Lymphadenopathy	195 ( 0.66%)	25561 (87.01%)	3621 (12.33%)
Emphysema	22399 (76.25%)	3775 (12.85%)	3203 (10.90%)
Atelectasis	24652 (83.92%)	4316 (14.69%)	409 ( 1.39%)
Lung Nodule	3210 (10.93%)	3978 (13.54%)	22189 (75.53%)
Lung Opacity	13026 (44.34%)	6437 (21.91%)	9914 (33.75%)
Pulmonary Fibrotic Sequela	22873 (77.86%)	2707 ( 9.21%)	3797 (12.93%)
Pleural Effusion	338 ( 1.15%)	26866 (91.45%)	2173 ( 7.40%)
Mosaic Attenuation Pattern	27800 (94.63%)	1546 ( 5.26%)	31 ( 0.11%)
Peribronchial Thickening	27089 (92.21%)	1931 ( 6.57%)	357 ( 1.22%)
Consolidation	23727 (80.77%)	5118 (17.42%)	532 ( 1.81%)
Bronchiectasis	25752 (87.66%)	2627 ( 8.94%)	998 ( 3.40%)
Interlobular Septal Thickening	26970 (91.81%)	2229 ( 7.59%)	178 ( 0.61%)

**Table S3:** Label distribution for AH-Abd dataset. The dataset contains 14,038 samples in total. The counts and percentages for Uncertain/missing (-1), Negative (0), and Positive (1) labels are shown.

Label	Uncertain/missing (-1)	Negative (0)	Positive (1)
Submucosal Edema	13870 (98.80%)	74 ( 0.53%)	94 ( 0.67%)
Renal Hypodensities	8213 (58.51%)	1874 (13.35%)	3951 (28.15%)
Aortic Valve Calcification	12570 (89.54%)	1439 (10.25%)	29 ( 0.21%)
Coronary Calcification	12562 (89.49%)	1365 ( 9.72%)	111 ( 0.79%)
Thrombosis	12233 (87.14%)	1454 (10.36%)	351 ( 2.50%)
Metastatic Disease	9076 (64.65%)	847 ( 6.03%)	4115 (29.31%)
Pancreatic Atrophy	7984 (56.87%)	5618 (40.02%)	436 ( 3.11%)
Renal Cyst	3596 (25.62%)	1505 (10.72%)	8937 (63.66%)
Osteopenia	13618 (97.01%)	395 ( 2.81%)	25 ( 0.18%)
Surgically Absent Gallbladder	7765 (55.31%)	4805 (34.23%)	1468 (10.46%)
Atelectasis	9214 (65.64%)	3982 (28.37%)	842 ( 6.00%)
Abdominal Aortic Aneurysm	10964 (78.10%)	3045 (21.69%)	29 ( 0.21%)
Anasarca	11587 (82.54%)	2432 (17.32%)	19 ( 0.14%)
Hiatal Hernia	11512 (82.01%)	2402 (17.11%)	124 ( 0.88%)
Lymphadenopathy	533 ( 3.80%)	8776 (62.52%)	4729 (33.69%)
Prostatomegaly	9365 (66.71%)	3403 (24.24%)	1270 ( 9.05%)
Biliary Ductal Dilation	3941 (28.07%)	8767 (62.45%)	1330 ( 9.47%)
Cardiomegaly	8926 (63.58%)	4980 (35.48%)	132 ( 0.94%)
Splenomegaly	1776 (12.65%)	11179 (79.63%)	1083 ( 7.71%)
Hepatomegaly	2311 (16.46%)	11445 (81.53%)	282 ( 2.01%)
Atherosclerosis	10938 (77.92%)	2564 (18.26%)	536 ( 3.82%)
Ascites	7435 (52.96%)	4517 (32.18%)	2086 (14.86%)
Pleural Effusion	4552 (32.43%)	8053 (57.37%)	1433 (10.21%)
Hepatic Steatosis	6801 (48.45%)	6232 (44.39%)	1005 ( 7.16%)
Appendicitis	6379 (45.44%)	7620 (54.28%)	39 ( 0.28%)
Gallstones	3355 (23.90%)	9166 (65.29%)	1517 (10.81%)
Hydronephrosis	8809 (62.75%)	4623 (32.93%)	606 ( 4.32%)
Bowel Obstruction	8956 (63.80%)	4943 (35.21%)	139 ( 0.99%)
Free Air	9157 (65.23%)	4788 (34.11%)	93 ( 0.66%)
Fracture	9062 (64.55%)	4610 (32.84%)	366 ( 2.61%)

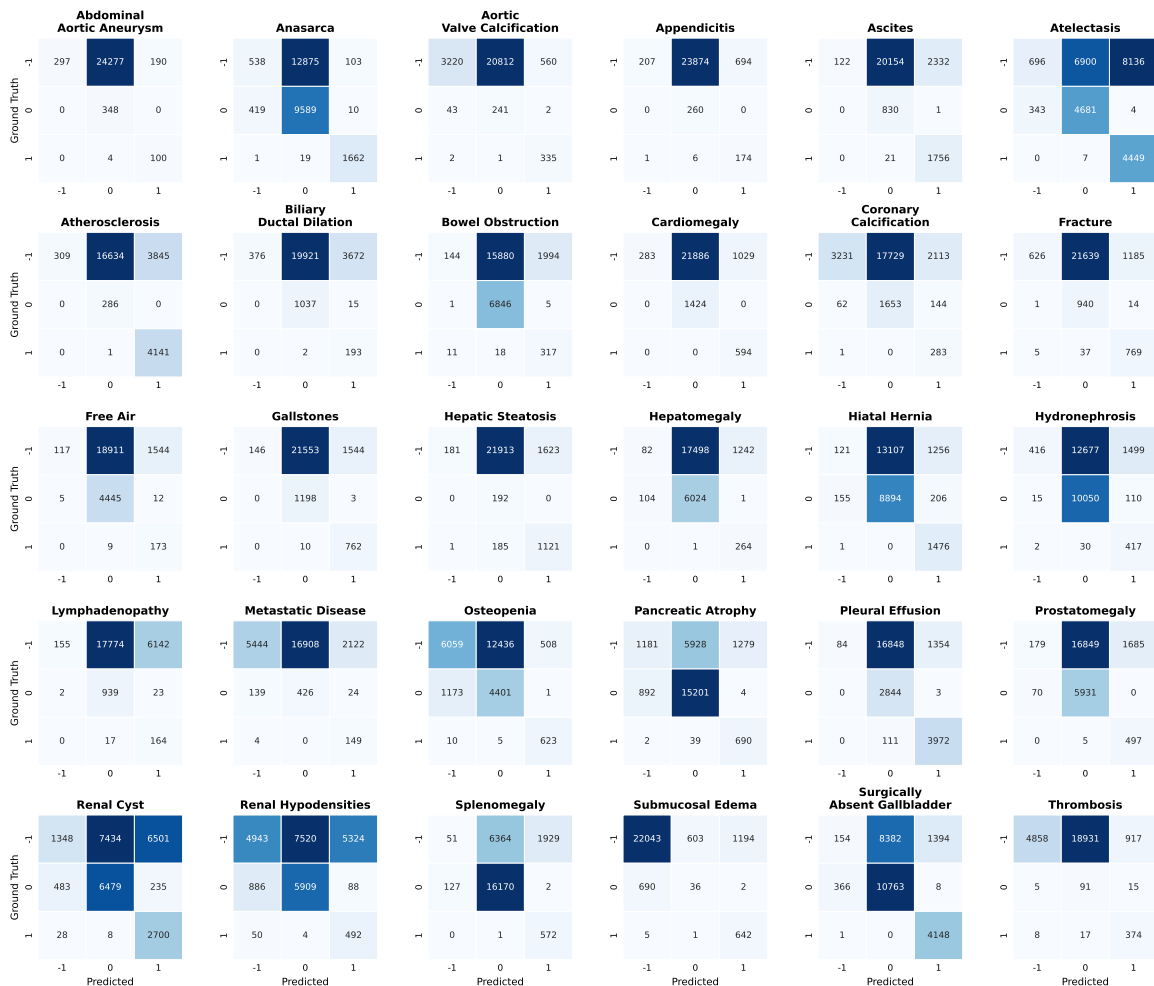
### C. Evaluation of LLM-extracted Labels

**Table S4: Evaluation of LLM-generated diagnostic labels.** The table assesses the agreement of LLM-generated labels with ground truth and their effectiveness for training vision encoders.

Agreement with Merlin official labels					
Evaluation Protocol	$\kappa$	Acc.	Prec.	Rec.	F1
Strict Match (w/ -1)	0.10	0.29	0.46	0.66	0.30
Ignore Uncertain (excl. -1)	0.94	0.98	0.95	0.98	0.96
Map Uncertain to Neg (-1→0)	0.43	0.91	0.33	0.97	0.46

Vision encoder performance (Merlin test set)						
Training Strategy	AUC	Acc.	Prec.	F1	Sens.	Spec.
Ignore Uncertain	85.78	86.30	61.38	86.39	69.65	81.22
Treat Uncertain as Neg (0)	84.39	84.27	59.52	84.66	70.71	78.02
Doubao (Ignore Uncertain)	87.49	88.30	70.57	87.85	69.65	83.18



**Figure S1: Confusion matrices comparing LLM-extracted labels against Merlin official labels.** The figure displays the confusion matrices for 30 abnormality categories. The rows represent the ground truth labels from the Merlin dataset, and the columns represent the labels extracted by the Doubao. The labels are defined as: 1 (present), 0 (absent), and -1 (uncertain/missing).

## D. Imaging equipment information

We summarize the imaging equipment and acquisition parameters for the datasets used in this study in Table S5.

**Table S5: Summary of imaging equipment and acquisition parameters.** This table provides an overview of the scanner manufacturers and models used across the different datasets. For AH-Chest, AH-Abd, AH-Knee, and AH-Spine, detailed statistics are derived from DICOM metadata.

Dataset	Manufacturer	Model	Slice Thickness (mm)	Tube Voltage (kVp)
CT-RATE	Philips (62%)	-	0.035 – 6.0	-
	Siemens (30%) GE (8%)			
Merlin	-	-	-	-
RAD-ChestCT	GE (57%)	-	0.6 – 0.625	-
	Siemens (43%)			
AH-Chest	GE (80%) Philips (20%)	Optima (49%)	0.625 – 5.0	80 – 140
		Brilliance (19%)		
		LightSpeed (18%)		
		Discovery (11%)		
AH-Abd	GE (100%)	Optima (45%)	0.625 – 5.0	100 – 140
		Discovery (40%)		
		Revolution (15%)		
AH-Knee (Private)	Siemens (88%) GE (12%)	Avanto (78%)	-	-
		Discovery MR750w (12%)		
		MAGNETOM Vida (10%)		
AH-Spine (Private)	Philips (50%) GE (45%) Siemens (5%)	Achieva (50%)	-	-
		Signa Voyager (44%)		
		MAGNETOM Vida (5%)		
		Discovery MR750w (1%)		

## E. Detailed results

**Table S6:** Detailed classification performance (AUC-ROC %) on AH-Chest dataset. Detailed results with all 18 abnormality categories.

Abnormality	BrgSA	GreenRFM (ours)
Atelectasis	53.4	73.8
Bronchiectasis	68.8	70.8
Consolidation	72.1	83.3
Coronary Artery Calcification	80.3	80.4
Emphysema	52.8	71.3
Hiatal Hernia	76.6	85.7
Interlobular Septal Thickening	52.5	74.0
Lung Nodule	54.6	59.7
Lung Opacity	50.6	75.1
Lymphadenopathy	52.0	69.8
Peribronchial Thickening	61.1	81.3
Pericardial Effusion	57.9	76.9
Pleural Effusion	69.8	77.5
Pulmonary Fibrotic Sequelae	54.5	63.9
AVG	61.2	74.5

**Table S7:** Detailed classification performance (AUC-ROC %) on AH-Abd dataset. Detailed results with all abnormality categories.

Abnormality	Merlin	GreenRFM (ours)
Thrombosis	65.0	71.5
Surgically absent gallbladder	56.1	87.3
Submucosal edema	70.2	73.3
Splenomegaly	60.8	77.1
Renal hypodensities	50.9	58.1
Renal cyst	51.8	59.1
Prostatomegaly	47.1	77.7
Pleural effusion	79.9	90.0
Pancreatic atrophy	58.5	77.6
Osteopenia	52.5	67.6
Metastatic disease	57.5	65.1
Lymphadenopathy	53.4	55.3
Hydronephrosis	60.9	85.5
Hiatal hernia	59.0	65.7
Hepatomegaly	64.1	76.4
Hepatic steatosis	56.0	86.7
Gallstones	53.3	67.5
Free air	61.0	55.3
Fracture	58.1	69.5
Coronary calcification	49.0	77.6
Cardiomegaly	70.8	86.4
Bowel obstruction	58.3	82.5
Biliary duct dilation	56.4	75.9
Atherosclerosis	58.9	64.3
Atelectasis	60.1	60.9
Ascites	72.9	73.4
Appendicitis	61.2	66.7
Aortic valve calcification	44.5	73.3
Anasarca	90.1	97.1
Abdominal aortic aneurysm	71.5	70.5
AVG	60.3	73.2

**Table S8:** Detailed classification performance (AUC-ROC %) on AH-Knee dataset. Detailed results with all 13 abnormality categories.

Abnormality	MRCLIP	GreenRFM (ours)
Medial meniscus injury	81.6	85.6
Lateral meniscus injury	72.8	71.6
Anterior cruciate ligament injury	65.8	84.3
Posterior cruciate ligament injury	55.5	72.0
Medial collateral ligament injury	82.1	84.7
Lateral collateral ligament injury	61.8	75.2
Articular cartilage defect, Osteochondral injury	80.9	86.9
Bone marrow edema, Contusion	77.7	87.3
Fracture Collapse	79.9	88.4
Joint effusion or Bakers cyst	69.2	52.3
Synovitis, Bursitis	56.1	60.7
Postoperative changes, Internal fixation	75.1	85.5
Degenerative osteoarthritis, Osteophytes	89.0	93.8
AVG	72.9	79.0

**Table S9:** Detailed classification performance (AUC-ROC %) on AH-Spine dataset. Detailed results with all 8 abnormality categories.

Abnormality	MRCLIP	GreenRFM (ours)
Intervertebral disc degeneration	74.8	86.5
Disc bulging	56.6	70.2
Disc herniation, Extrusion	61.1	79.2
Spondylolisthesis	73.7	78.3
Spinal canal or foraminal stenosis	57.7	73.2
Endplate changes, Schmorls nodes, Modic changes	72.0	74.1
Compression fracture, Acute bone contusion	91.4	95.8
Postoperative changes, Internal fixation, Bone graft fusion	76.3	88.8
AVG	70.5	80.8

## F. LLM prompts for visual description extraction

To extract visual descriptions from radiology reports for the ablation study, we utilized the following system prompt. Notably, unlike our diagnostic label extraction which explicitly models uncertainty (class -1), we employed a deterministic binary schema (0/1) for visual patterns. We instructed the LLM to output 1 only when a pattern was *explicitly and clearly* described, and 0 otherwise. This decision relies on the distinction between observation and interpretation: while diagnostic conclusions often carry uncertainty, visual findings (e.g., “high attenuation”) are typically factual observations. By enforcing a strict binary output, we ensure that the visual supervisory signal is high-precision, minimizing noise from ambiguous descriptions.

### System Prompt: Visual Description Extraction

You are an experienced chest radiologist. Review each non-contrast chest CT report and determine whether the following visual patterns are explicitly described. If a pattern is clearly present, output 1; if it is not mentioned or the description is inconclusive, output 0. Multiple patterns can be present simultaneously.

Visual patterns to evaluate (binary flags in this exact order):

- Density patterns -
  1. High-attenuation focus (density\_high)
  2. Low-attenuation focus (density\_low)
  3. Mixed-attenuation focus (density\_mixed)
- Morphology patterns -
  4. Nodular opacity (morphology\_nodular)
  5. Patchy opacity (morphology\_patchy)
  6. Linear/stripe-like opacity (morphology\_linear)
  7. Reticular/network-like opacity (morphology\_reticular)
- Distribution patterns -
  8. Focal distribution (distribution\_focal)
  9. Diffuse distribution (distribution\_diffuse)
  10. Bilateral symmetric distribution (distribution\_bilateral\_symmetric)
  11. Unilateral distribution (distribution\_unilateral)

Output format: exactly eleven comma-separated binary digits (0 or 1) matching the order above, with no additional text or punctuation.

Example: 0,1,0,0,0,1,0,1,0,0,0

## G. LLM prompts and code for diagnostic label extraction

To ensure a full reproducibility, we provide the exact system prompts and a simplified Python implementation used to extract structured diagnostic labels from radiology reports.

### G.1. Prompt for 30-class diagnostic label extraction (Merlin/AH-Abd)

#### System Prompt: 30-Class Diagnostic Label Extraction

You are a board-certified radiologist specializing in thoracic imaging.

Task

Classify the chest/abdomen CT report for the following 30 findings, in the exact order listed:

1. submucosal\_edema

2. renal\_hypodensities
3. aortic\_valve\_calcification
4. coronary\_calcification
5. thrombosis
6. metastatic\_disease
7. pancreatic\_atrophy
8. renal\_cyst
9. osteopenia
10. surgically\_absent\_gallbladder
11. atelectasis
12. abdominal\_aortic\_aneurysm
13. anasarca
14. hiatal\_hernia
15. lymphadenopathy
16. prostatomegaly
17. biliary\_ductal\_dilation
18. cardiomegaly
19. splenomegaly
20. hepatomegaly
21. atherosclerosis
22. ascites
23. pleural\_effusion
24. hepatic\_steatosis
25. appendicitis
26. gallstones
27. hydronephrosis
28. bowel\_obstruction
29. free\_air
30. fracture

Labeling rules

- Output a single line of 30 comma-separated values.
- Use 1 if the finding is explicitly present.
- Use 0 if the finding is explicitly ruled out or absent.
- Use -1 if the report is ambiguous, uncertain, or lacks information.

Only return the comma-separated numbers.

Example:

0,1,-1,-1,1,-1,-1,-1,-1,-1,0,0,0,0,1,0,0,0,-1,0,0,1,0,0,0,0,0,0,0

## G.2. Prompt for 18-class diagnostic label extraction (CT-RATE/AH-Chest)

### System Prompt: 18-Class Diagnostic Label Extraction

You are a board-certified radiologist specializing in thoracic imaging.

#### Task

Classify the chest/abdomen CT report for the following 18 findings, in the exact order listed:

1. medical material
2. arterial wall calcification
3. cardiomegaly
4. pericardial effusion
5. coronary artery wall calcification
6. hiatal hernia
7. lymphadenopathy

8. emphysema
9. atelectasis
10. lung nodule
11. lung opacity
12. pulmonary fibrotic sequela
13. pleural effusion
14. mosaic attenuation pattern
15. peribronchial thickening
16. consolidation
17. bronchiectasis
18. interlobular septal thickening

#### Labeling rules

- Output a single line of 18 comma-separated values.
- Use 1 if the finding is explicitly present.
- Use 0 if the finding is explicitly ruled out or absent.
- Use -1 if the report is ambiguous, uncertain, or lacks information.

Only return the comma-separated numbers.

Example:

0,1,-1,-1,1,-1,-1,-1,-1,-1,0,0,0,0,1,0,0,0

### G.3. Label extraction and verification workflow

To ensure the reliability of the extracted labels, we implement a rigorous verification loop (Fig. S2). The process involves: 1. **Extraction**: The LLM is prompted to generate a structured string of comma-separated integers. 2. **Format verification**: The output is parsed to ensure that it contains exactly  $N$  tokens (18 for CT-RATE, 30 for Merlin) and that every token is a valid class identifier  $\{-1, 0, 1\}$ . 3. **Error handling**: If the output fails verification, the request is retried with exponential backoff up to 3 times. This filters out hallucinated formats or incomplete generations. Samples that fail all retry attempts are logged for manual review to ensure data integrity.

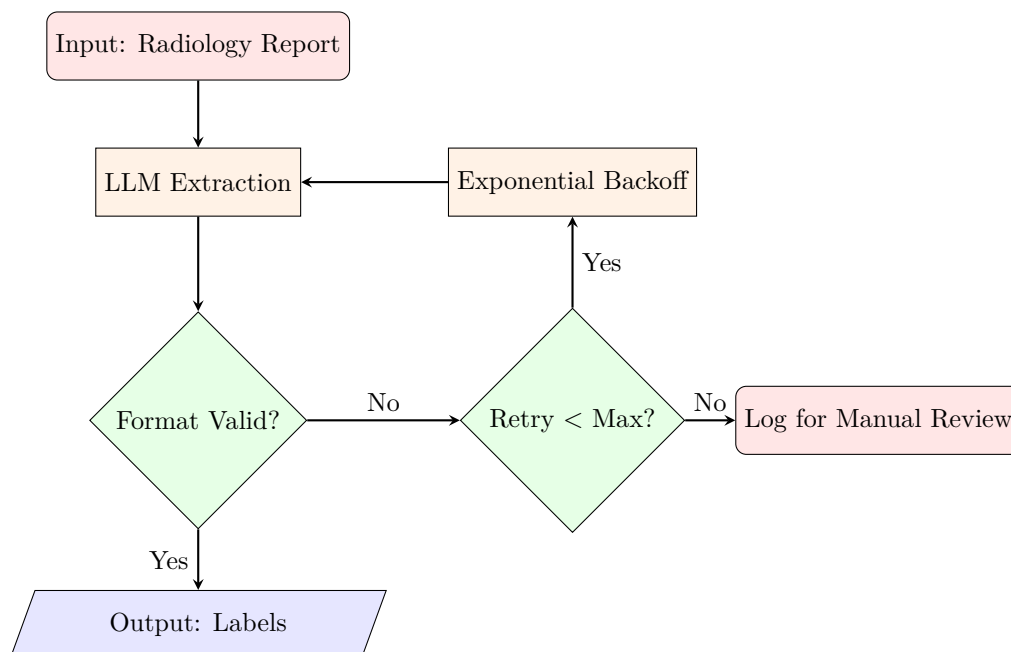


**Figure S2: Schematic of the LLM-based label extraction and verification pipeline.** The workflow ensures that only syntactically valid label sequences are accepted. Invalid outputs trigger a retry mechanism to maximize data utilization while maintaining structure integrity.

## H. Grad-CAM visualizations

We use Grad-CAM to visualize the image regions activated by the corresponding text prompts in the CLIP model. We observe discernible patterns in the model's attention. We have selected a set of representative samples to illustrate these behaviors, as shown below.

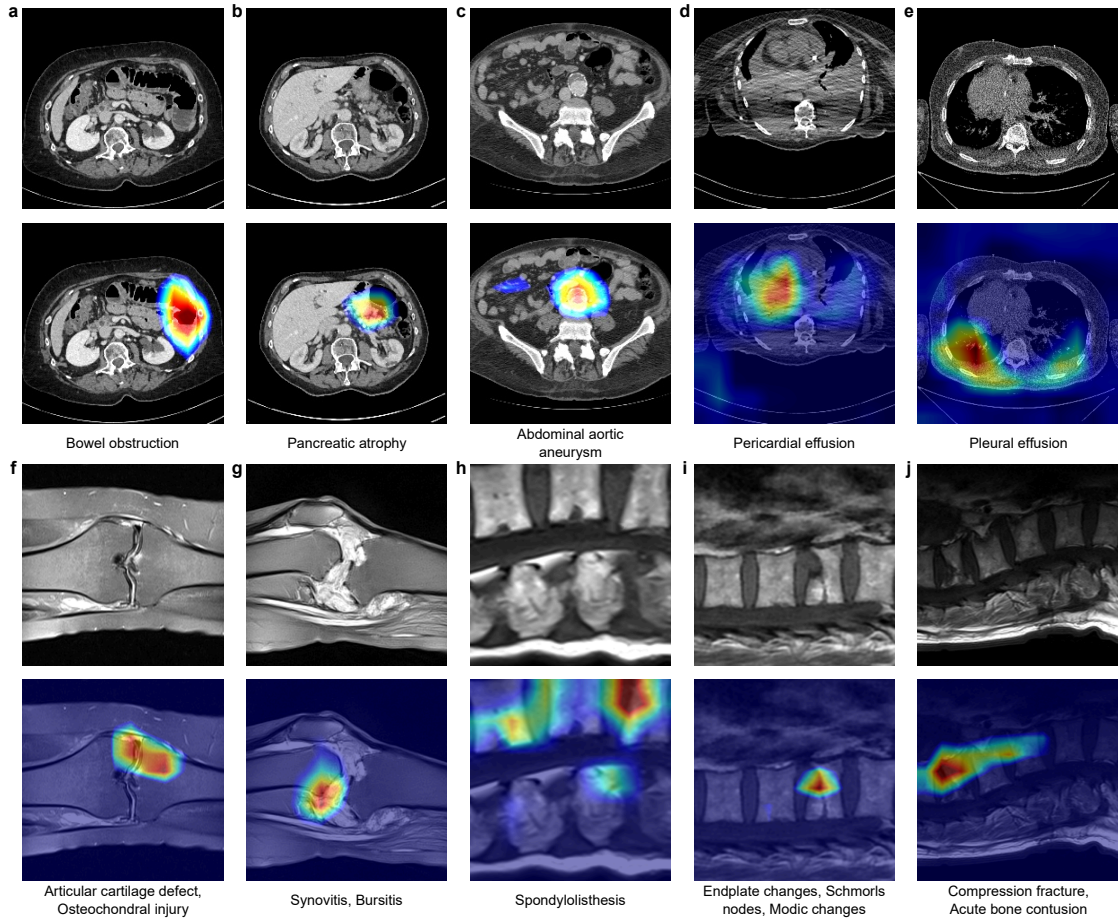


**Figure S3: Visualization of correct pathology localization using Grad-CAM heatmaps.** The figure displays representative cases where the model successfully identified the region of interest. The top rows show the original cross-sectional imaging (CT or MRI), and the bottom rows show the corresponding class activation maps superimposed on the original images, with red regions indicating high diagnostic weight. (a) Bowel obstruction. (b) Pancreatic atrophy. (c) Abdominal aortic aneurysm. (d) Pericardial effusion. (e) Pleural effusion. (f) Articular cartilage defect, osteochondral injury. (g) Synovitis, bursitis. (h) Spondylolisthesis. (i) Endplate changes, Schmorl's nodes, and Modic changes. (j) Compression fracture, acute bone contusion.

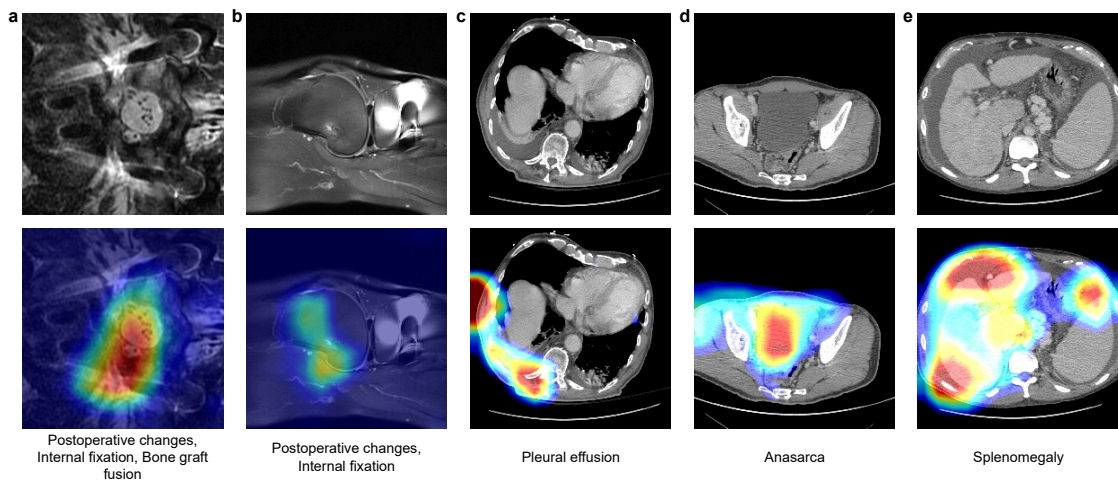


**Figure S4: Failure modes and misinterpretation of Grad-CAM heatmaps.** The figure highlights cases where the model failed to localize the primary pathology or focused on anatomically irrelevant regions. (a-b) Postoperative changes (Knee & Spine): The model consistently failed to activate regions with internal fixation or bone grafts. (c) Ascites/Pleural Effusion confusion: The model displayed ambiguity in distinguishing fluid compartments, likely due to the similar radiodensity of pleural and peritoneal fluids. (d) Anasarca: In cases of anasarca, the model often disproportionately directs high attention to the bladder, misinterpreting high-contrast fluid accumulation as the target feature. (e) Splenomegaly: In cases of splenomegaly, the model often simultaneously focuses on the liver; this might suggest the model relies on comparative organ sizing or hepatosplenomegaly co-occurrence patterns.